Actively Conformable Aerodynamic Surfaces

by

Mark Alexander Kepets

S. B., Aeronautics and Astronautics, Massachusetts Institute of Technology, Cambridge, Massachusetts (2000)

Submitted to the Department of Aeronautics and Astronautics
in partial fulfillment of the requirements for the degree of

MASTER OF SCIENCE IN AERONAUTICS AND ASTRONAUTICS

at the

MASSACHUSETTS INSTITUTE OF TECHNOLOGY

May 2002

June 2002

© Massachusetts Institute of Technology 2002. All rights reserved.

Author_____
Department of Aeronautics and Astronautics
May 20, 2002

Certified by_____
Carlos E. S. Cesnik
Visiting Associate Professor of Aeronautics and Astronautics
Thesis Supervisor

Accepted by_____
Wallace E. Vander Velde
Professor of Aeronautics and Astronautics
Chair, Committee on Graduate Students

MASSACHUSETTS INSTITUTE OF TECHNOLOGY
AUG 1 3 2002
LIBRARIES
AERO

Actively Conformable Aerodynamic Surfaces

by

Mark Alexander Kepets

Submitted to the Department of Aeronautics and Astronautics
on May 20, 2002, in partial fulfillment of the
requirements for the degree of
Master of Science in Aeronautics and Astronautics

Abstract

An integrally twisting wing was developed as means of implementing roll control in a WASP class UAV. The study began by investigating various control options including the use of conventional control surfaces as well as a slotted spoiler concept. The actuation of the wing was accomplished by embedding anisotropic strain actuators within the composite construction. These offer several distinct advantages over the conventional actuators including savings in weight, mechanical complexity, g-hardening, as well as control authority. Active Fiber Composites were oriented at $\pm 45^{\circ}$ in order to twist the wing along its span. A finite element model of the wing was constructed and validated in NASTRAN in order to model the effects of the AFC as well as to maximize the tip twist angle. Aeroelastic, inertial, and aerodynamic models were implemented within this framework in order to optimize the composite layup of the wing while still meeting the given launch and aerostability requirements. Once an optimal design was obtained, a prototype wing was manufactured with six AFC actuators embedded within the composite surface. A flexible circuit was also designed and fabricated in order to provide a low profile solution for powering the actuators. Electromechanical bench tests were carried out and the performance of the wing was characterized. The frequency response of the wing and the voltage twist transfer functions were obtained and compared with the finite element model. The results showed good correlation with the expected twist values falling within 7% of the finite element model. Only one actuator survived the maximum expected operating voltage. The remaining actuators failed during the experiment resulting in lower than expected actuation values. Initial indications show that the circuit as well as the connections are the probable source of failure in four out of the five actuator failures. The remaining failure appears to be a result of failure within the actuator itself.

Thesis Supervisor: Carlos E. S. Cesnik
Title: Visiting Associate Professor of Aeronautics and Astronautics

Acknowledgments

This thesis would not have been possible without the guidance and assistance of many people. First, I would like to thank my advisor, Carlos Cesnik. His advice these past years on this thesis as well as on my academic direction has been invaluable.

I am especially grateful to Draper Laboratory for their financial support. In particular, I would like to thank Sean George for his guidance and insight on this project as well as the other research projects that I have had the privilege to work with him on.

I would like to acknowledge everyone who provided academic as well as moral support for this project. Thanks to John Kane for his assistance and patience in the lab. I would also like to thank my labmates, Dong Jin Shim, Torrey Radcliffe, Kevin Turner, Jeremy Gregory, Linda Mendenhall, and Seth Kessler for their help and willingness to answer my questions. A special thanks to Chris Gouldstone for his perpetually twisted humor and his ability to always put things into perspective.

I would like to thank Marie Stuppard, the glue that holds together this department, for looking after me these past five years and always being there to listen.

I could not have done this work without the support of my friends who have helped keep me sane these past few years. To Chuck Toye, the best bad influence a friend could have. To Dave, for showing us the way. To Roo, for his intensity, integrity, and intelligence. It's true, It's true. To Brian, whose family name ain't the best in the navy. To Erin, for putting up with us during lunch. To Padraig, for bringing me back to my roots. To Shannon, leader of the squirtle gang. To the Shen, for all the food and taking the fish tank.

Finally, and most importantly, I would like to thank my family. This thesis would not have been possible without their continued love and support.

Contents

Abstract **2**

Acknowledgments **3**

1 Introduction **10**

1.1 Motivation 10

1.2 WASP 11

1.3 Present Work 13

2 Preliminary Actuation Mechanisms Study **15**

2.1 Performance Requirements 15

2.2 Discrete Control Surfaces 16

2.2.1 Piezoelectric Benders 17

2.2.2 X-frame Actuator 17

2.3 Distributed Actuation 19

2.4 Slotted Spoileron 21

2.5 Actuator Selection 21

3 Analysis of the Integral Twist Concept **23**

3.1 Aerodynamic Analysis 23

3.2 Structural Analysis 25

3.2.1 Equivalent Thermal Load 26

3.2.2 Twist Model 27

3.2.3 Modelling Validation 31

3.2.4 Buckling Model . . . 32
3.3 Aeroelastic Analysis . . . 34
3.4 Final Design . . . 36

4 Fabrication **38**
4.1 Wing Mold . . . 38
4.2 Foam Cores . . . 39
4.3 Active Elements . . . 40
4.3.1 Flexible Circuit . . . 40
4.3.2 Assembly . . . 42
4.4 Final Assembly . . . 43

5 Testing and Results **48**
5.1 Bench Testing . . . 48
5.2 Results . . . 51
5.2.1 Actuator Free Strain Characterization . . . 51
5.2.2 Twist Actuation . . . 52
5.2.3 Resonance Frequency Characterization . . . 55
5.2.4 Powering to Design Conditions . . . 56

6 Conclusions **62**
6.1 Summary . . . 62
6.2 Recommendations for Future Work . . . 63

Bibliography **66**

A Slotted Spoiler **69**
A.1 Fabrication . . . 69
A.2 Testing . . . 70
A.3 Results . . . 72

B MATLAB Script **77**

List of Figures

1-1 Wide Area Surveillance Projectile. 11

1-2 WASP mission profile. 12

2-1 Piezoelectric bender 17

2-2 X-frame actuator *(Source: MIT AMSL web site).* 18

2-3 Spoileron configuration. 19

2-4 Active Fiber Composite 20

2-5 Schematic representation of electric field in the fibers. 20

3-1 Treftz plane from AVL modelling. 24

3-2 Base WASP layout and layup 25

3-3 Base WASP finite element model 26

3-4 Active Fiber Composite patch geometry 27

3-5 Spanwise actuator placement 28

3-6 Actuator placement options 28

3-7 Finite element model of the active WASP wing 29

3-8 ATR Cross-section and layup 31

3-9 Geometry and material of box beam BB1 32

3-10 Geometry and material of box beam BB2. 32

3-11 Stowed configuration of WASP (*courtesy of Draper Laboratory*) 33

3-12 Buckling model of wing 34

3-13 Tip deflection of wing under aero loads 35

3-14 WASP wing final cross-sectional layup 36

3-15 WASP wing actuator placement 37

4-1 Wing mold 39
4-2 Foam core 40
4-3 Flexible circuit template 41
4-4 Flexible circuit drawing 41
4-5 Circuit and actuators 43
4-6 Wing mold and actuators 45
4-7 Outer ply and upper surface actuators 45
4-8 2 composite plies and foam cores prior to folding 45
4-9 Lower surface actuators 46
4-10 Wing prior to closing of the mold 46
4-11 WASP wing tip after fabrication 47

5-1 Laser vibrometer 49
5-2 Aluminum clamp 49
5-3 Displacement sensor measurement 50
5-4 Displacement sensor setup 50
5-5 Free strain of actuators 51
5-6 Actuator pack numbering scheme 52
5-7 Vibrometer displacement measurements of active wing excited at 350 V p-p/5 Hz 54
5-8 Voltage-twist relationship at 5 Hz 55
5-9 Frequency response of wing 57
5-10 Laser displacement sensors setup 58
5-11 High voltage response of wing at 0.5 Hz (actuator 1 only) 60
5-12 High voltage response of wing at 0.5 Hz (actuator 5 only) 60
5-13 Deformed shape of wing (one actuator only) 61

A-1 Hole layout 70
A-2 Final wing with wax filled holes 70

A-3 Tunnel setup 71
A-4 Lift measurements at 27 m/s 73
A-5 Lift measurements at 18 m/s 73
A-6 Torque measurements at 27 m/s 74
A-7 Torque measurements at 18 m/s 74
A-8 Net roll measurements at 27 m/s 75
A-9 Net roll measurements at 18 m/s 75
A-10 Baseline lift measurements at 27 m/s 76

List of Tables

1.1 Aileron characteristics 12

2.1 WASP characteristics 16

3.1 Actuator placement results 28
3.2 Material properties of AS4/3501-6 composite system and AFC actuators . . 30
3.3 Material properties of Rohacell 31 30
3.4 Results of final design 36

4.1 Actuator capacitance measurements 42

5.1 Capacitance and resistance measurements for first failed packs 53
5.2 NASTRAN correlation 54
5.3 Frequency response of wing 56
5.4 AFC behavior- high voltage 58
5.5 Final actuator capacitance measurements 59

A.1 Test matrix for the slotted wing (runs are at 18 m/s and 27 m/s) 71

Chapter 1

Introduction

1.1 Motivation

With the invention of the airplane, the need has always existed to implement control in a flight vehicle. In the early days of flight, this was accomplished by warping the wings, creating an asymmetric lift distribution and a net rolling force. The low speeds of early airplanes allowed for the successful implementation of this mechanism. However, as the speed of flight increased, the torsional flexibility required for wing warping became a liability, resulting in divergence and aeroelastic instabilities. As a result, wings became stiffer and heavier. The stiffer wings made warping unfeasible, resulting in the use of ailerons and other discrete control surfaces.

Recently, high performance small scale Unmanned Air Vehicles (UAV) have become increasingly more prominent in tactical applications. Vehicles such as Predator and Pioneer have risen to the forefront of military tactics [1]. Other new developments, such as the Wide Area Surveillance Projectile (WASP), have size and maneuverability requirements that present unique challenges to traditional roll control mechanisms. The need for high performance presented by these vehicles coupled with the advent of new materials allow for the reexamination of a variety of mechanisms for implementing roll control.

1.2 WASP

The Wide Area Surveillance Projectile (Figure 1-1) was conceived as a means to reduce the risk and cost associated in acquiring time critical reconnaissance data. WASP was commenced as a joint venture between MIT and the Charles Stark Draper Laboratory. The goal of the project was to develop an autonomous, low cost, expendable vehicle capable of being launched from a standard artillery round using cameras to track ground targets and conduct battle damage assessment. The unique launch environment of the vehicle necessitates the use of lightweight structures capable of handling the extreme g-loads of launch, while the vehicle maintains sufficient maneuverability and endurance to accomplish its mission.

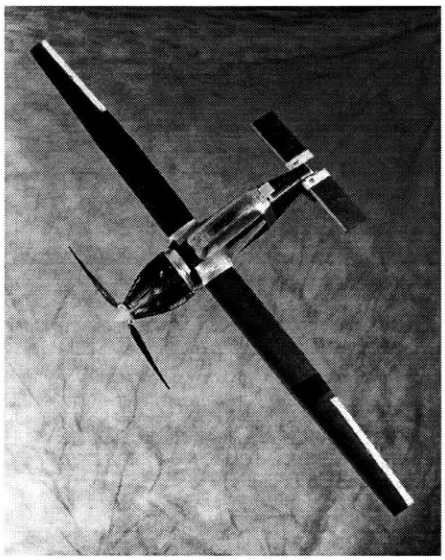


Figure 1-1: Wide Area Surveillance Projectile.

The mission profile of the WASP (Figure 1-2) presents a unique challenge to the design of a roll control actuation scheme. The size constraint of the artillery shell prompted the use of segmented wings in order to efficiently package the flyer. The current WASP wing calls for a carbon fiber wing 0.62 m in span with a midspan hinge located 0.3 m from the wing tip.

Several different actuation schemes could be implemented in order to provide adequate roll control for the WASP flier over its mission profile. The conventional approach would be the implementation of ailerons on the outboard segment of the wings. The initial design of

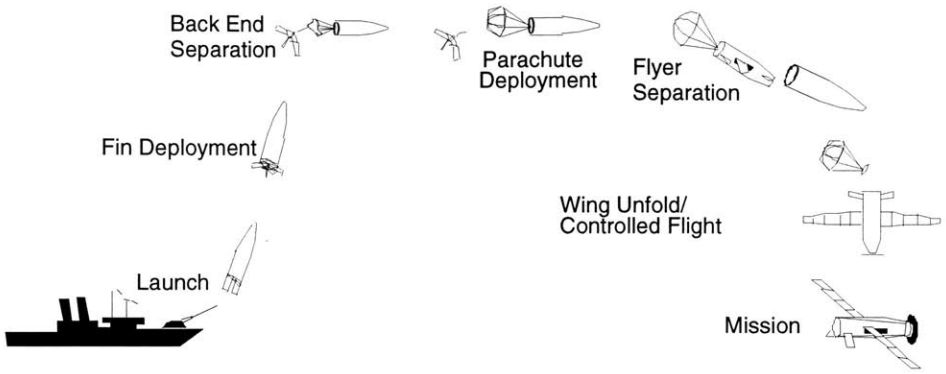


Figure 1-2: WASP mission profile.

the control surfaces called for the use of conventional aileron surfaces with a chord of 15.24 mm and a span of 254 mm. The basic characteristics are summarized in Table 1.1.

Table 1.1: Aileron characteristics

Chord	15.24 mm
Length(2x)	254 mm
Deflection range	+/- 15 degrees
Max torque	1.36 N-m
Max Roll Rate	203 deg/s

Traditionally, these control surfaces are actuated with discrete servos. The servos are typically connected to the surfaces by way of linkages and bearings. The initial design of the ailerons was intended as a stopgap measure and could not be implemented in the final vehicle. The small size of WASP increases the dynamic frequencies of the vehicle, exceeding the bandwidth of discrete servo-actuators. In addition, the actuation mechanism for this scheme called for the placement of the actuators outboard on the wing. This location would interfere with the folding mechanism as well as incur a drag penalty on the aerodynamics of the flyer. It was proposed to place the actuators inside the vehicle fuselage while running linkage arms outboard to the control surfaces. However, this would require the linkages to traverse an open gap across the hinge when the vehicle is stowed. It was also believed that the high g-loads experienced by the vehicle during launch would cause the required bearings and linkages to fail. Consequently, an alternate actuation scheme for these surfaces was

necessary.

The second approach to implement roll control has its origins as far back as the Wright flier. The wings of the WASP would be actively warped in flight. This scheme would allow for controlling the lift differentially between the two wings by locally changing the angle of attack, and consequently the lift. However, unlike the Wright flier, the WASP wing cannot use cables and pulleys to twist the wing. The midspan hinge as well as the high-g launch environment present a challenge to the implementation of this control method.

The third major approach involves the use of a spoiler concept. By actuating the spoiler, lift may be reduced locally on one of the wings. Consequently a net roll moment may be achieved providing suitable control for the vehicle. Two spoiler concepts were examined. The first concept was a discrete control surface located on the aft section of the wing that would disrupt the air flow over the foil. However, this configuration faces many of the same issues that a discrete aileron surface does regarding actuation mechanisms. The second design for the spoiler calls for the actuation of apertures to allow for air to flow through the body of the wing. This would nullify the pressure difference over the foil section resulting in a decrease in lift.

1.3 Present Work

Active materials, particularly piezoelectric ones, present a possible solution to the challenges facing the above actuation schemes. Their small size and high bandwidth are ideally suited, allowing them to be packaged within the primary structure of the wing, g-hardening the actuator. This location for the actuators also eliminates linkages and bearings that may fail under the initial launch load as well as eliminate any drag penalty associated with having the actuators in the free stream flow. Incorporating active materials within the structure allows them to be used as primary structural elements resulting in an overall savings in weight.

This thesis will examine the implementation of active materials as a roll control mechanism in the WASP vehicle. To accomplish this, models were constructed and experiments carried out to demonstrate the feasibility of active materials in a composite structure. Chapter 2 discusses previous research in the use of active materials in aerospace structures. Chap-

ter 3 discusses the analytical procedures including structural, aerodynamic, and aeroelastic modelling of the wing. Chapter 4 details the fabrication of the composite structure and the integration of the active materials. Chapter 5 describes the experimental setups including electromechanical testing. This chapter also discusses the test results and evaluates the accuracy of the modelling. Chapter 6 summarizes the conclusions arrived from this study as well as recommendations to for future work.

Chapter 2

Preliminary Actuation Mechanisms Study

This chapter discusses preliminary studies into the use of active materials as a means of controlling the aerodynamics of a vehicle.

2.1 Performance Requirements

The target aerodynamic performance for the WASP vehicle was set by the Draper Laboratory [2]. A minimum roll rate of 30 deg/s was required. This value was determined based on the WASP mission profile that calls for loitering reconnaissance with no large roll angles. Based on the WASP characteristics, outlined in Table 2.1, this translates into a required roll torque of 0.428 N-m. A separate static roll torque goal was also set. This upper limit was designed to counter potential static roll torque sources that would act on the vehicle. These external roll sources would need to be corrected by the roll actuators in order to maintain the trim of the vehicle. The sources may be broken down into three major categories:

1. reaction to propeller torque
2. lateral gust disturbances
3. mis-alignment of wing surfaces

Table 2.1: WASP characteristics

WASP design velocity	26.8 m/s
Wing area (S_w)	0.08 m^2
Wing span (b)	1.27 m
WASP design dynamic pressure (q)	415.5 N/m^2
WASP damping coefficient (C_{lp})	0.75
WASP design minimum roll rate	30 deg/s
Minimum roll torque (30 deg/s)	0.428 N-m
Roll torque goal (30 deg/s + roll offset)	1.769 N-m

The contribution from each was determined to be 0.60 N-m, 0.27 N-m, and 0.47 N-m respectively [2]. These values were obtained based on assumptions for the cruise power and propeller RPM as well as a maximum offset of 0.5° between wings and a maximum side slip disturbance of 10°. The effect of these sources results in a maximum roll torque goal of 1.769 N-m. Aerodynamic stability requirements also exist. In order to maintain the stability of the vehicle, the static bending deflection of the wings under steady load should not exceed 13°. This corresponds to a tip deflection of 3.05 cm. The flutter boundary of the vehicle was also set to $1.2 \cdot V_{NE}$ (velocity never exceed) =(1.2)(40.23 m/s)=48.28 m/s. This speed was determined based on the cruise velocity of the vehicle as well as the requirement that stability be maintained through a 13.41 m/s gust.

2.2 Discrete Control Surfaces

Primarily, three types of actuation schemes were examined using active materials embedded within the primary structure. The first method calls for the use of active materials to actuate a discrete control surface. The basic mechanism would entail the use of a piezoelectric bender or a mechanically amplified piezoelectric stack to actuate an aileron. Piezoelectric materials exhibit coupling between electrical and mechanical behavior. The application of an electric field to the material will cause a mechanical deformation. Conversely, applied deformation will result in the flow of charge through the material. The actuator would be mounted internal to the wing structure and would connect to the control surface directly. The location

of the actuator as well as the minimization of linkages makes this configuration naturally g-hardened. In addition, by placing the actuators within the primary wing structure, the wing would be able to fold completely allowing WASP to be packaged within the geometric constraints of the delivery vehicle.

2.2.1 Piezoelectric Benders

Piezoelectric benders have been used in controlling vibrations in helicopter rotor blades via a discrete flap [3]. Bench tests by Hall and Prechtl [4] have demonstrated flap deflections up to 11.5° under no load conditions. Analysis indicated that under load, the maximum deflection would be 6.7°. The piezoelectric bender actuator consists of a multilayered piezoelectric sheets bonded to a very thin metal shim (Brass, Aluminum). Equal but opposite fields are applied to the piezoelectric sheets on either side of the shim resulting in a pure bending moment. The resulting tip displacement is mechanically amplified to provide actuation for the flap. The piezoelectric bender actuator has the advantage of being simple to implement, however, the amount of control authority scales with the length of the actuator.

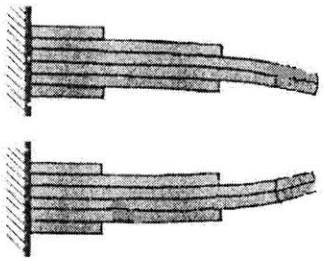


Figure 2-1: Piezoelectric bender

2.2.2 X-frame Actuator

To overcome the limitations of the simple bender actuator, different amplification schemes have been presented in literature [5-10]. Prechtl and Hall [11] have developed a high efficiency discrete servo-flap actuator. The X-frame actuator has demonstrated a mass efficiency between 18% and 31% with a mechanical efficiency between 38% and 50%. This scheme relies on the use of a non-active frame mechanism for amplifying the piezoelectric stack motion.

The X-frame consists of two piezoelectric stacks simultaneously actuating against two steel frames. A roller pin is situated between the two frames allowing for relative rotation of the frames. The small angle of the frames relative to the stack axis results in a geometric stroke amplification of approximately 15. A compressive pre-stress is required to maintain contact between the frame and the stack. This is achieved by placing a tensile load along the load path of the actuator. In practical applications this was accomplished via a spring connected between the actuator and the flap [11].

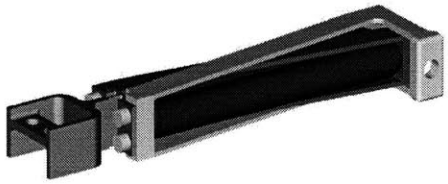


Figure 2-2: X-frame actuator *(Source: MIT AMSL web site).*

Additional work has been conducted by Hall and Tzianetopoulou [12] to further refine this actuation scheme. The double X-frame actuator incorporates a number of design innovations over the original X-frame design. The volume of active material within the actuator has been increased. The pre-stress of the actuator stacks are applied internally. This avoids the disadvantage of the original X-frame causing a hard-over deflection of the flap in case of actuator failure.

The X-frame could be mechanically coupled to actuate an aileron surface in a similar fashion as the piezo-bender. The X-frame could also be used to actuate a spoileron concept (Figure 2-3). This concept recovers approximately 60% to 70% of the effectiveness of an aileron [13], while being relatively less complex mechanically. The actuator is well suited for this configuration. The X-frame would be situated at the hinge point. At this location, the required actuation is one that is high force with a small stroke, ideal for piezoceramic materials.

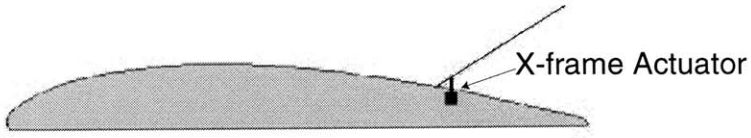


Figure 2-3: Spoileron configuration.

2.3 Distributed Actuation

The second actuation scheme involves the use of distributed actuators. Distributed actuation follows two distinct paths. The first involves the use of sheets of piezoelectric material to actuate the aerodynamic surface. The work of Bernhard and Chopra [14] uses a distributed actuation scheme to actuate a discrete control surface. The tips of a segmented rotor blade are actively pitched via a piezo-driven bending-torsion coupled beam. Piezo elements mounted on the upper and lower surface of the beam are actuated in a similar manner of the piezo-bender to produce spanwise bending in the beam. The structural bend-twist couple of the beam results in an induced twist which is used to pitch the blade tips of the rotor. One distinct advantage exists in this system compared to a piezo-bender is that the entire wing span can be used for actuation. Since the actuation stroke scales with length, much larger actuations may be achieved without mechanical amplification. This system, however, demonstrates poor energy efficiency inherent in elastically coupled systems. Preliminary performance of a Mach-scale blade indicates blade-tip pitch deflections of 1.75°. This performance comes at the cost of a significant weight penalty.

Work by Lazarus and Crawley [15, 16] and Nam and Kim [17] focused on the use of distributed piezoelectric wafer actuators as a means of flutter suppression of a composite lifting surface. Similarly, Ehlers and Weisshaar [18] studied the use of embedded piezoelectric actuators to change wing lift and divergence dynamic pressure by deforming the shape of the wing.

The second path of distributed actuation involves the use of Piezoelectric Fiber Composites (PFC) [19]. Unlike traditional piezoelectric actuators that rely on piezoelectric wafers, this material combines fine ceramic fibers in a soft matrix to provide load mechanisms that

increase tolerance to damage by providing a load path around fiber cracks. This represents an improvement over ceramic wafer based actuators that are subject to macroscopic damage resulting from cracks in the material.

An example of PFC are Active Fiber Composites (AFC) [19]. AFCs are used with an interdigitated electrode pattern (Figure 2-4). This pattern orients the electrical field along the length of the fiber taking advantage of the directional actuation properties of the material (Figure 2-5). Application of an electric field causes in-plane actuation in the direction of the fibers.

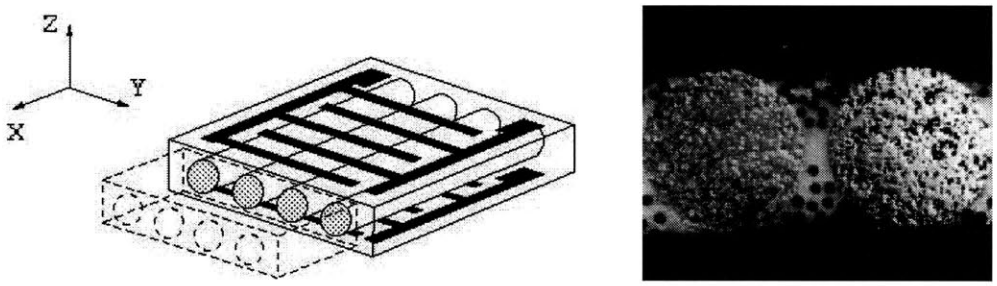


Figure 2-4: Active Fiber Composite

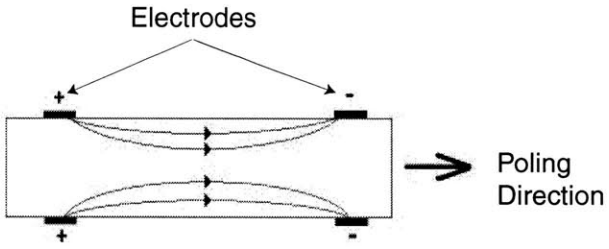


Figure 2-5: Schematic representation of electric field in the fibers.

Extensive work has been done by Bent and Hagood [19] on the effectiveness of the interdigitated electrode pattern over standard Piezoelectric Fiber Composites. Values of free strain constants show a fivefold increase of AFC over PFC. When these materials are oriented at a $\pm 45°$ to the blade span, they may be actuated to produce a pure twisting moment. The moment causes the lifting surface to twist affecting the overall lift distribution. These high strain actuators have been used extensively in the development of integrally-twist helicopter rotors.

MIT and NASA have built an integrally actuated rotor blade known as the Active Twist Rotor (ATR) [20]. The project successfully demonstrated the feasibility of using AFC as a means of actuation to achieve independent blade control on a helicopter rotor system. A twist rate of 1.5°/m was achieved during forward flight tests at NASA Transonic Dynamics Tunnel [21].

2.4 Slotted Spoileron

A third actuation scheme was also examined. The method called for opening and closing small ports through the thickness of the wing. By controlling the flow of air through the cross-section, the pressure differential across the airfoil may be locally nullified, resulting in a decrease in lift. By actuating these ports differentially between the two wings, a net rolling moment may be produced. The concept was tested experimentally and the results are presented in detail in Appendix A.

2.5 Actuator Selection

Discrete actuation schemes and the slotted wing concept were not pursued further in this thesis. The lack of an applicable actuator in the slotted wing concept prohibited the implementation of a flight capable roll mechanism. Regarding the discrete actuators, research in the literature has demonstrated the successful implementation of these systems and consequently, the main issue for this study would be that of packaging the actuators within the wing. In addition, these actuation schemes still rely on mechanical linkages to join the actuator to the flap. Consequently, they have the potential for failing during the high-g launch environment. The relative high cost of the actuators also made their use prohibitive. Current cost of a X-frame actuator is estimated at approximately $10,000/actuator [22]. Finally, Koratkar and Chopra [3] have also shown that a major source of performance degradation for this type of actuation scheme is friction created at the blade flap interface. On the other hand, distributed actuation presents itself as an efficient and viable option for use in the WASP-class wing. The high bandwidth of piezoelectric-embedded actuators enables

robust effective control of the vehicle. Additionally, by integrating the actuators to the primary structure, discrete servos, linkages, and bearings are no longer necessary resulting in a savings in weight and mechanical complexity. The relatively high strain rates exhibited by AFC packs as well as their ability to be easily incorporated within the structural layup of the wing makes them the most promising actuation scheme for implementing roll control for a WASP-class vehicle.

Chapter 3

Analysis of the Integral Twist Concept

This chapter outlines the analytical procedures used to optimally design a WASP-class wing for use with an integral twist actuation scheme. Aerodynamic modelling was conducted to determine the wing twist needed to meet the given performance requirements. A static structural model of the wing was constructed and validated to optimize the layup in order to achieve the desired twist rate using AFC packs. The aeroelastic response of the wing was studied. MSC/NASTRAN was chosen for the analyses for its wide range of toolboxes. This range allowed for the study of the twist, aeroelastic, and the inertial loading within a single model.

3.1 Aerodynamic Analysis

A baseline model of the WASP was constructed in the Athena Vortex Lattice (AVL) [23]. The coordinate points of the foil cross-section were input and a constant cross-section wing was assumed. Initial analysis was conducted assuming a constant twist rate. A roll torque coefficient was derived by normalizing the required roll torques by the parameter $q \cdot S \cdot b$ where q is the dynamic pressure, S the wing area and b the wing span. Based on the requirements, the coefficient of roll (C_r) was determined to be 0.0093 for the lower bound, and 0.0384 for

the worst roll torque condition.

Initial results from AVL indicated that a tip twist angle of 0.6° (based on a linear twist distribution along the wing span) was necessary to satisfy the minimum roll torque requirement. This translates into a twist rate of 0.95 deg/m. For the roll torque goal, a tip twist angle of 2.4° was determined with a corresponding twist rate of 3.87 deg/m. These values were calculated using the assumption that the wings would be actuated asymmetrically, i.e., one wing would twist up at an angle of 2.4°, while the opposite wing would twist down 2.4°. The differential aerodynamic load on the wings shown in Figure 3-1 contributes to the roll moment on the vehicle.

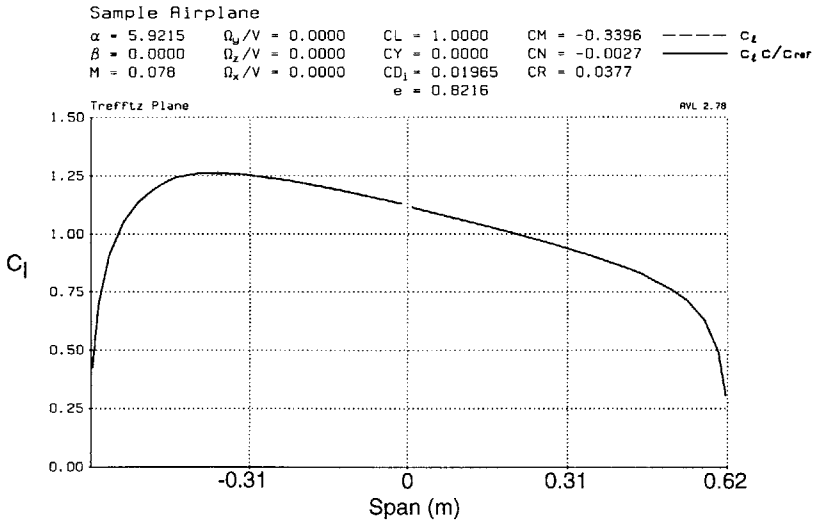


Figure 3-1: Treftz plane from AVL modelling.

Once the required twist angles were determined, an appropriate structural model could determine the optimal placement and number of the individual actuators as well as the structural layup of the composite wing.

3.2 Structural Analysis

A finite element model of the wing with integral anisotropic piezoelectric actuators was developed to analyze the twisting of the wing. The baseline WASP layup was initially considered [24].

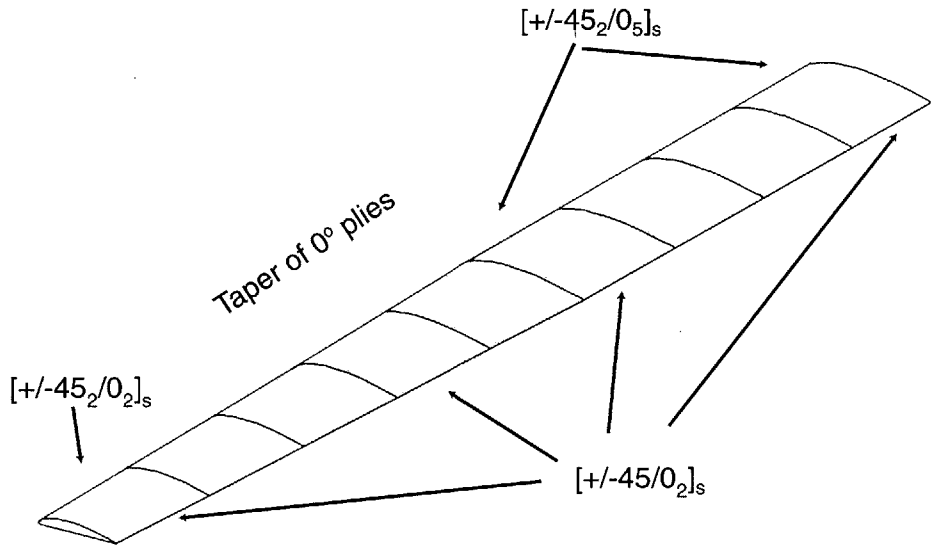


Figure 3-2: Base WASP layout and layup

The original wing design called for a taper in chord as well as thickness as shown in Figure 3-2. The layup was uniform along the lower surface of the wing $[\pm 45/0_2]_s$. The upper surface of the wing tapered from a base layup of $[\pm 45_2/0_5]_s$ to $[\pm 45_2/0_2]_s$ at the tip. The geometry was eventually changed in favor of a wing with constant cross-section along the span. The switch to this new configuration proved to be beneficial to the integral actuation scheme. The additional chord length allowed for more area to be covered with active materials, increasing the control authority of the wing.

The initial model was comprised of an airfoil shell discretized into 9 spanwise segments (Figure 3-3). The discretization was included to allow for the spanwise taper in thickness that was present in the initial WASP layup. The chordwise taper in thickness was not modelled.

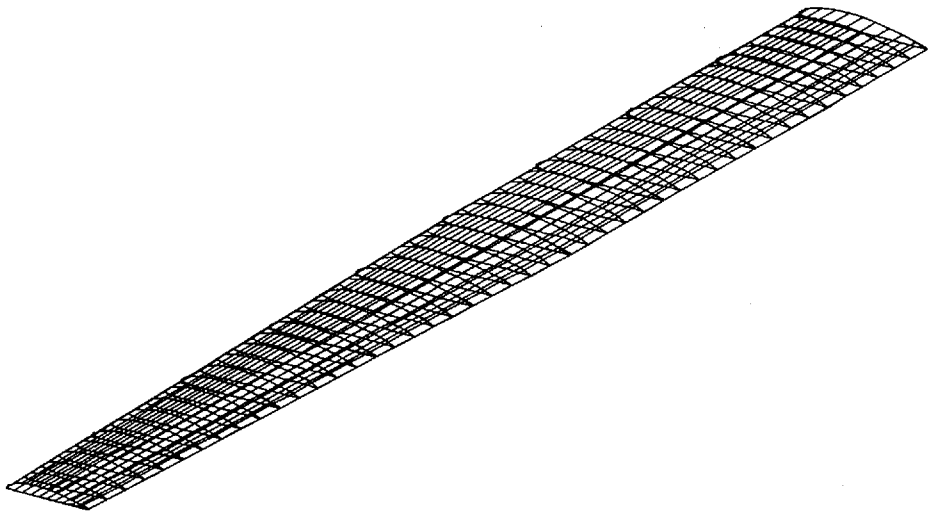


Figure 3-3: Base WASP finite element model

3.2.1 Equivalent Thermal Load

The piezoelectric effect of the AFC patches was modelled using an equivalent thermal load. The induced free strain of the piezoceramic material is assumed to behave linearly and proportionally to the applied electric field, and is given by

$$\varepsilon_{33} = d_{33} \cdot E \tag{3.1}$$

where E is the applied electric field and d_{33} is the piezoelectric coefficient in the poling direction. The linearity of this relationship can be properly modelled in NASTRAN by applying an equivalent thermal load. Once the free strain of the actuators is known, a value for the coefficient of thermal expansion, α, can be input for the AFC material to model d_{33} and a thermal load, ΔT, applied to simulate the applied electric field.

$$\varepsilon_{33} = d_{33} \cdot E \sim \alpha \cdot \Delta T \tag{3.2}$$

In this equation α is one of the anisotropic coefficients of thermal expansion. The direction of the coefficient is oriented along the length of the fiber. This ensures that the equivalent thermal load applies the strain in the same direction as the AFC actuators.

3.2.2 Twist Model

In order to determine the feasibility of the integral twist configuration, a baseline case was first considered to determine a reference twist authority that would be provided by the AFC patches. Initially, the entire upper and lower surface of the wing was covered with a single layer of AFC material. The resultant tip twist angle was 0.15°. The baseline layup of the original wing was extremely stiff in both torsion and bending. Without compromising any of the wing performance requirements, the off-axis plies were removed to reduce the torsional stiffness. A resultant tip twist angle of 1.35° was obtained. These results indicated that a feasible design exists that satisfies the desired actuation range of the wing. From this point, the layup of the wing could be optimized for roll performance while remaining within the flutter and static deflection boundaries outlined from aerodynamic analyses.

The model was then refined to accurately model the new geometry of the wing planform as well as the geometric shape of the actuators. The actuators chosen for this project were similar to the ones used by Schmidt [25] and Wickramasinghe [26] in support to the DARPA/Boeing/MIT Active Helicopter Rotor Program. This was done in order to save time as well as additional cost associated with customizing the actuators to the WASP wing. As a result, the actuators were not ideally sized for this application. The geometry of the actuators are shown in Figure 3-4.

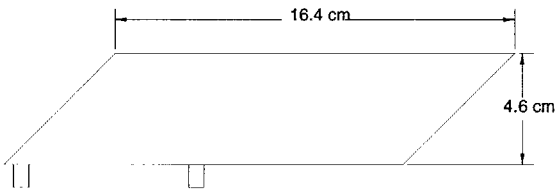


Figure 3-4: Active Fiber Composite patch geometry

Due to the length of the actuators, only six could be placed on the wing (Figure 3-5), three on the upper and another three on the lower surfaces. This configuration resulted in a gap of approximately 14.6 cm where there would be no active material. Studies were conducted in both AVL as well as NASTRAN to determine whether the actuators should be placed more outboard or inboard on the wing in order to maximize the roll moment produced (Figure 3-6). Working with a base layup of three uni-directional 0° plies, the two actuator

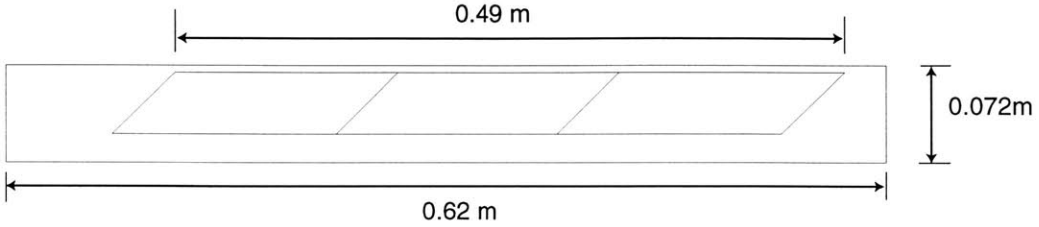


Figure 3-5: Spanwise actuator placement

placements were examined. The placement of the actuators inboard assumes that the wing will remain at a constant twist angle from the end of the actuator packs out to the wing tip. In both cases, the placement of the midspan hinge was not taken into account. The analysis assumes that the hinge would act as a rigid body, transmitting the twist angle between the two segments of the wing. The results are summarized in Table 3.1

Table 3.1: Actuator placement results

Location	Tip Twist	C_r
Inboard	$\pm 1.18°$	0.0175
Outboard	$\pm$ 1.04°	0.0103

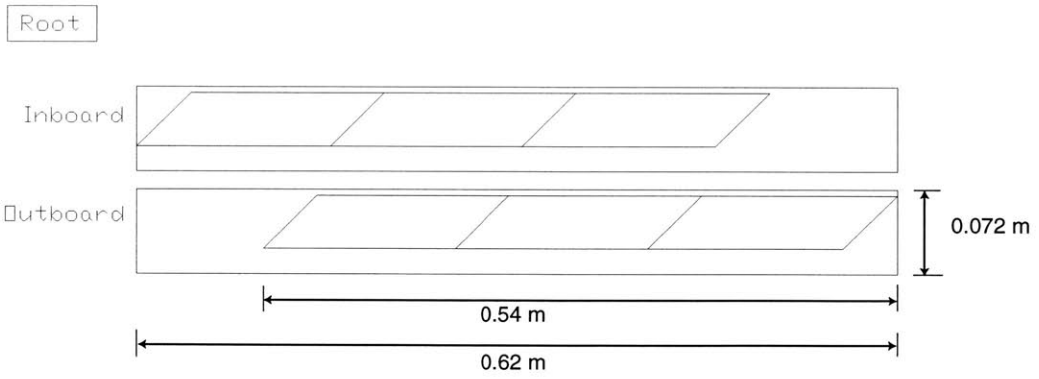


Figure 3-6: Actuator placement options

Placement of the actuators inboard represents an overall improvement in performance for a given number of actuators and power of 70%.

The AFC actuators were placed one layer deep from the surface of the composite. This was done in an attempt to maximize the applied torque generated by the AFC by maximizing

the moment arm from the center of the foil while still having a layer of composite material protecting them from the external environment.

The resulting model consisted of 522 nodes and 756 elements (Figure 3-7). A total of 504 shell elements (QUAD 4) were used to model the composite structure including the AFC actuators. A combination of solid elements were used to model the core of the wing using 56 wedge elements near the leading and trailing edges with 196 tetrahedron elements for the center section of the core.

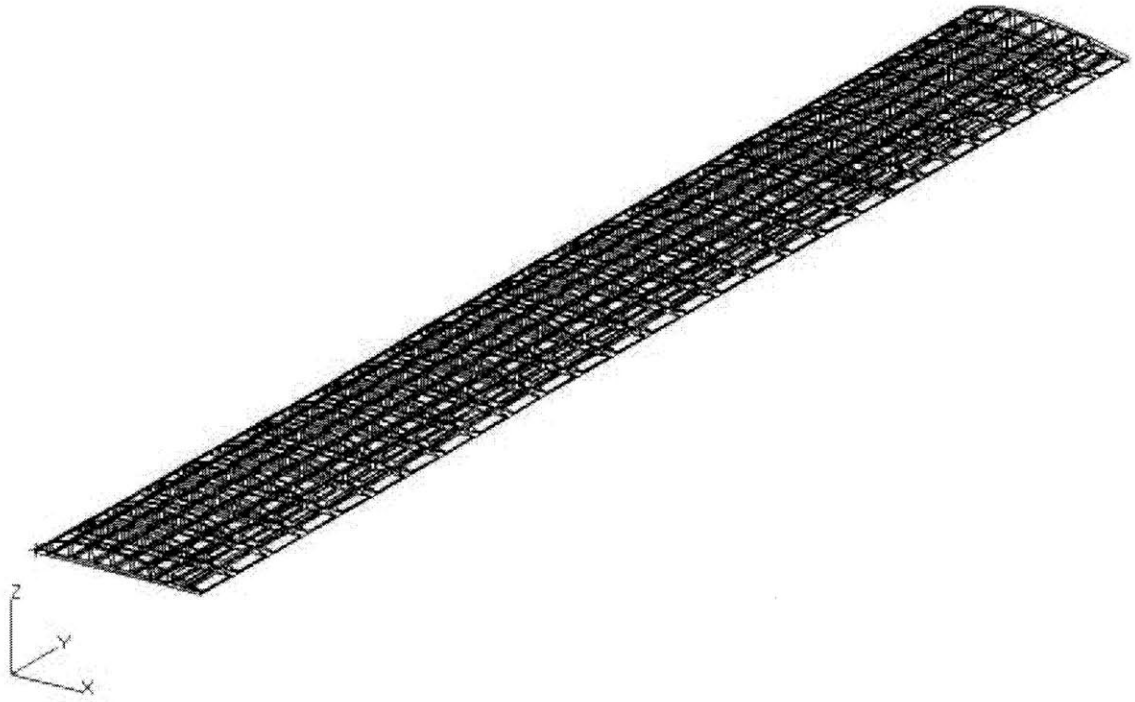


Figure 3-7: Finite element model of the active WASP wing

The AFC piezoelectric properties were input as coefficients of thermal expansion. The values of the d_{33} were normalized along with the applied thermal load to produce an equivalent 1000 $\mu\varepsilon$. Only the AFC material was given a non-zero thermal coefficient. This ensures that no other material would be affected by the application of the thermal load. The composite material used was AS4/3501-6 composite system. The material properties for the AFC and the AS4/3501-6 are outlined in Table 3.2.

Rohacell foam was chosen as the core material. The selection of Rohacell was a result

Table 3.2: Material properties of AS4/3501-6 composite system and AFC actuators

Property	AS4/3501-6	AFC
E_L	143 GPa	20 GPa
E_T	9.81 GPa	14.5 GPa
ν_{LT}	0.3	0.21
G_{LT}	5.58 GPa	4 GPa
thickness	0.127 mm	0.3429 mm
density	1514 kg/m^3	4096 kg/m^3

of its high temperature properties allowing it to be safely used in the autoclave during the fabrication process. Several different grades of Rohacell were examined to determine the lightest foam that would ensure the correct aerodynamic shape. The primary function of the foam core is to provide the proper back pressure during fabrication to ensure the composite material conforms to the shape of the mold. Rohacell 31 was selected experimentally for the core material. The mechanical properties of Rohacell 31 are outlined in Table 3.3.

Table 3.3: Material properties of Rohacell 31

Property	Rohacell 31
E	36 MPa
G	14 GPa
density	30 kg/m^3

The model was constrained at the root with a clamped boundary condition. A uniform thermal load was applied to the structure and the corresponding deflections were measured. In order to determine the twist angle, two nodes were selected at the tip of the wing. The difference between the leading and trailing edge deflections at the wing tip was measured from NASTRAN. This value was used to compute the twist angle at the tip of the wing. The chord length of the wing remains constant during actuation.

3.2.3 Modelling Validation

In order to ensure that the methodology used during the modelling was accurate, several test cases were run to compare with different analysis codes. The Active Twist Rotor blade described in Ref [20] was modelled in NASTRAN. The blade consisted of a 1-m long uniform beam with a NACA 0012 cross section of 0.11-m chord. The rotor was discretized into five regions in NASTRAN. The fairing, web, and nose were modelled separately along with the active regions along the upper and lower surfaces (Figure 3-8). The core of the rotor was not modelled as it was not included in the analysis conducted in [20]. The analysis used a two-cell thin-walled closed-section composite beam with anisotropic plies embedded in it. Preliminary results determined the twist rate for the ATR is 1.8°/m. Analysis conducted in NASTRAN yielded a rate of 1.72°/m. This corresponds to an error of approximately 4.6%.

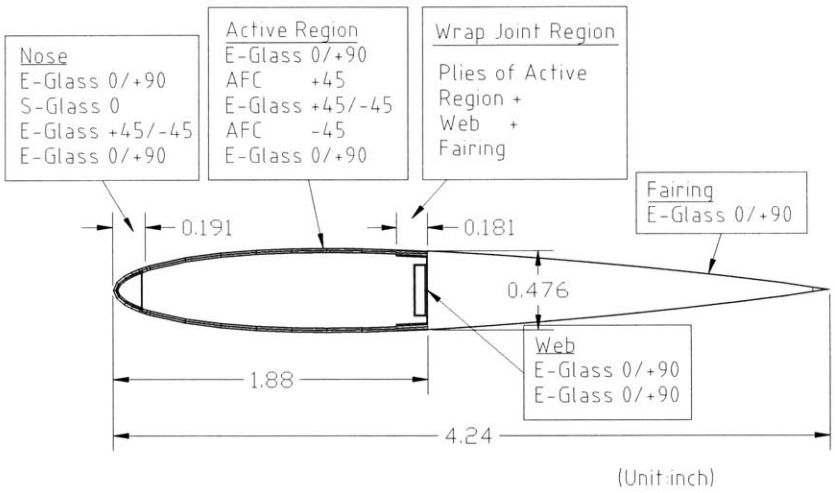


Figure 3-8: ATR Cross-section and layup (reproduced from [20], p. 106)

Additional analysis was conducted with an active composite box beam. Two box beams were modelled in VABS-A by Ortega-Morales and Cesnik [27]. Variational Asymptotical Beam Sectional Analysis (VABS-A) is a cross sectional analysis tool that calculates the beam stiffness and actuation constants for a cross section with arbitrary geometry made of anisotropic material. These beams consisted of a square cross section of 25-mm sides. The layups of the individual beams is shown in Figures 3-9 and 3-10.

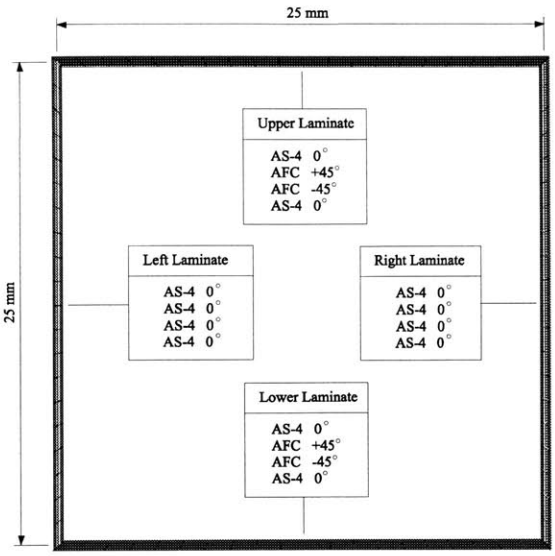


Figure 3-9: Geometry and material of box beam BB1

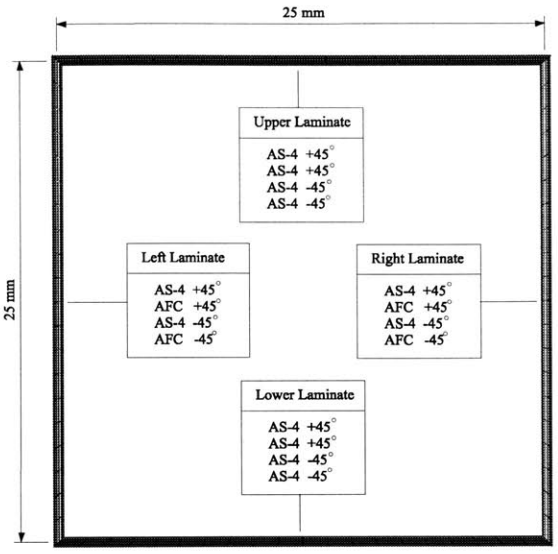


Figure 3-10: Geometry and material of box beam BB2.

The beams were modelled in NASTRAN and the results compared. A predicted twist rate of 1.87°/m was obtained for the unidirectional beam compared with 1.76°/m from VABS-A. This corresponds to an error of 6.23%. In the second case, a value of 0.737°/m was calculated compared to 0.814°/m from VABS-A. This corresponds to −9.35% difference. Based on the good correlation between two very distinct methods of calculating the actuation results, the NASTRAN model was deemed appropriate and validated for the present study.

3.2.4 Buckling Model

A nonlinear static analysis was also conducted to determine the effect of the initial launch acceleration on the redesigned layup. In the stowed configuration, the wing is folded and supported from a hinge at the root as shown in Figure 3-11. The outboard section is folded such that the mid span hinge is located towards the tail of the flyer, with the wing tip being on level with the root hinge. This results in the outboard segment of the wing being supported solely at the mid span hinge, leading to a compressive load during launch. The initial acceleration loads were provided by Draper Laboratory based on previous gun launch data. The specifications called for the wing to be able to survive an initial setback load of 16,000 g.

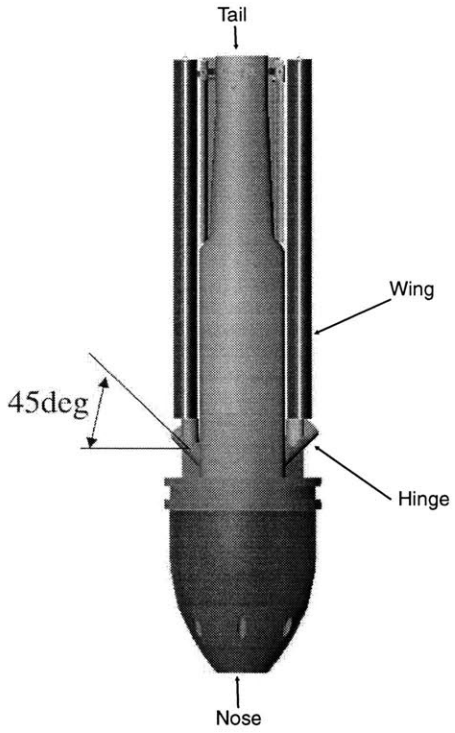


Figure 3-11: Stowed configuration of WASP (*courtesy of Draper Laboratory*)

A half-wing model was constructed in NASTRAN to simulate the outboard segment only as shown in Figure 3-12. This model was constructed in a similar fashion as the twist model. The root of the wing was cantilevered and an inertial load of 16,000 g applied to the structure. A failure model was implemented to ensure that the applied loads did not exceed the allowable levels for interlaminar shear stresses as well as the maximum allowable strain for the composite materials. In the case of the AFC layers, the allowable strain levels corresponded to the maximum strain the AFC fibers can withstand without depoling. Depoling the fibers would render the AFC actuators useless. This would constitute a failure of the structure despite the maintained structural integrity of the wing. Results from NASTRAN indicated that the wing would survive the launch with minimal out of plane deflections. A maximum value of 0.1956 mm was calculated for the out of plane deflection with a corresponding compression of 0.08 mm. This corresponds to a maximum strain of 600 $\mu\varepsilon$ while the allowable strains for the AFC fibers is 2500 $\mu\varepsilon$.

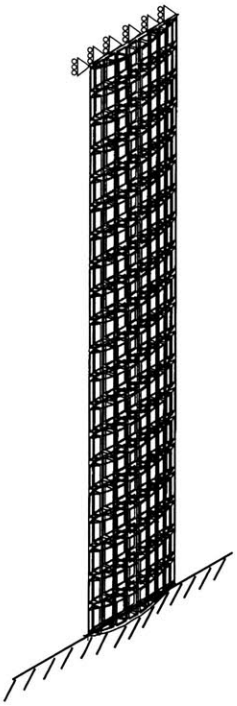


Figure 3-12: Buckling model of wing

3.3 Aeroelastic Analysis

Once the placement of the actuators on the wing was determined, and the methodology validated, the laminate was modified in an attempt to minimize the overall stiffness and weight. Off-axis plies were removed from the upper and lower surfaces in an attempt to reduce the torsional stiffness of the wing. Once all the off-axis plies were removed, it was determined that the wing was still excessively stiff in torsion and bending. As a result, 0° were removed in an attempt to further reduce the overall stiffness. The number of plies that could safely be removed from the layup ended up being limited by the aeroelastic requirements on the flyer. These requirements set a limit on the flutter speed as well as the maximum induced dihedral of the wings under steady aerodynamic loading.

To determine the aeroelastic performance of the wing, a model was created in NASTRAN using the *aeroelastics* package. The aerodynamic model utilizes a flat plate doublet-lattice method. The aerodynamics are coupled to the structure through spline elements. These spline elements serve to transmit load and deflection values between the aerodynamic plate

and the structural mesh. The flutter analysis was performed using the p-k flutter method. A modified Givens method was used to extract the eigenvalues and corresponding eigenvectors from the system.

Successive off-axis plies were removed and the flutter speed of the wing calculated. The finalized design consisted of a uniform layup with two uni-directional 0° plies on both the upper and lower surfaces. The flutter speed for this configuration was calculated to be 75 m/s. Decreasing the thickness of the layup beyond this point resulted in a flutter speed that was within the flight envelope of the WASP.

This configuration was then loaded statically under cruise conditions to determine the steady state induced dihedral of the wings. The wings were also subjected to an actuation load in order to determine the worst case steady state deflection. Figure 3-13 summarizes the results. For the steady cruise case, the maximum deflection is 0.93 cm. For the actuated case, the maximum value is 1.5 cm. This increase is due to the increased pitch of the wing as well as the resultant increase in the aerodynamic forces. Both these values are well below the 3.05 cm prescribed limit.

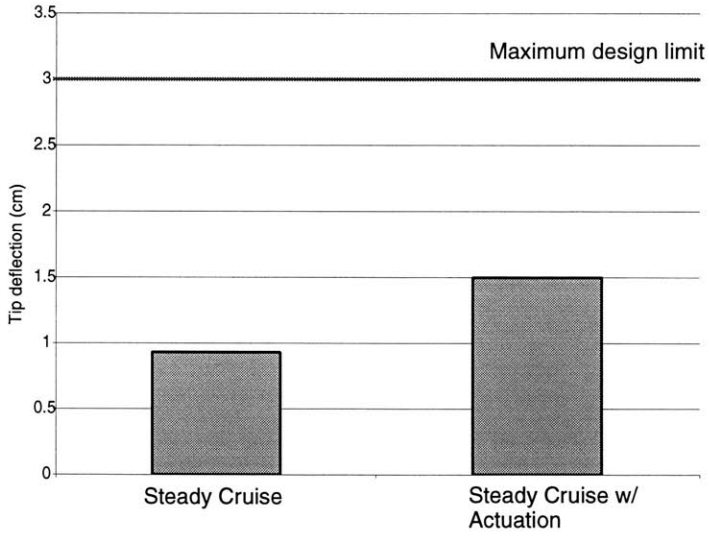


Figure 3-13: Tip deflection of wing under aero loads

3.4 Final Design

The final design for the WASP wing obtained from the analysis consisted of a uniform cross-section with no taper in either thickness or chord. The cross-section is represented in Figure 3-14. The design consisted of a uniform layup with two uni-directional 0° plies on both the upper and lower surfaces.

Rohacell 31 was selected as the material for the core of the wing. 6 actuators were placed along the span of the wing, three actuators on either surface. The actuators were placed inboard starting at the root leaving a region of approximately 14.6 cm with no actuation at the tip of the wing as shown in Figure 3-15. The main characteristics of the wing are summarized in Table 3.4

Table 3.4: Results of final design

Property	Final Design	Requirement
Tip twist Angle (±)	1.55°	0.59°-2.41°
Flutter Speed	75 m/s	$\geq$ 54 m/s
Induced Dihedral	1.5 cm	$\leq$ 3.0 cm

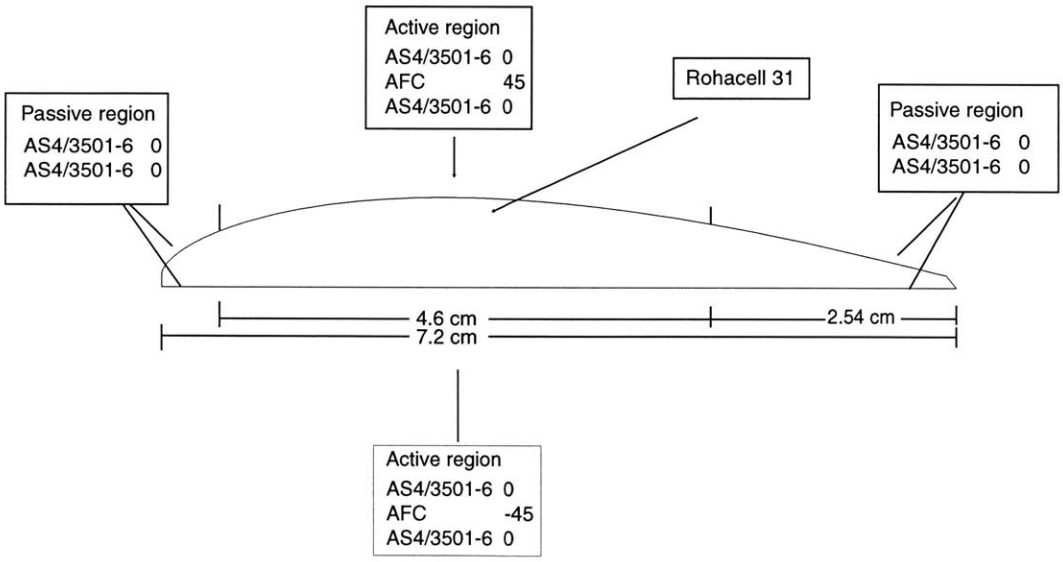


Figure 3-14: WASP wing final cross-sectional layup

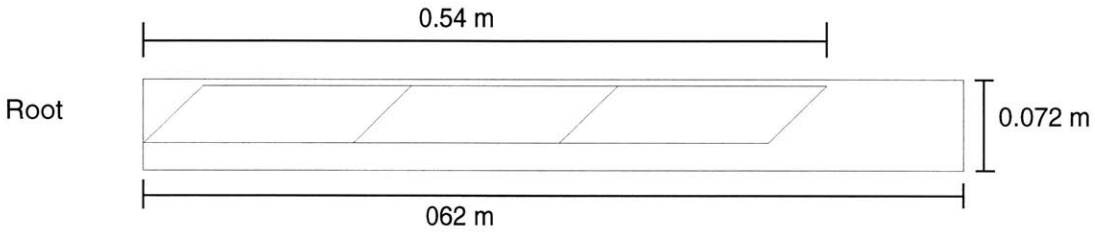


Figure 3-15: WASP wing actuator placement

Chapter 4

Fabrication

This chapter describes the fabrication of the active wing used to demonstrate the wing warping concept. The prototype wing was manufactured according to the final design described in Chapter 3.

4.1 Wing Mold

The redesigned planform and manufacturing procedure of the wing required the fabrication of a new mold. The previous design of the WASP wing involved a wet layup. The individual surfaces of the wing were manufactured and then bonded together with a secondary cure. For the new design, the upper and lower surfaces were co-cured resulting in a solid cross-section.

The new design called for a two piece closed mold as shown in Figure 4-1. The mold was oversized to allow for an additional 3.8-cm of clearance along the length of the wing. This additional length provided a clamping surface for the wing to be mounted. The mold was split along the lower surface of the foil. The aerodynamic shape of the foil was machined into a 2.54-cm thick piece of aluminum and capped with two aluminum end plates. The second piece of the mold was machined flat to ensure good surface finish on the composite. Clearance holes were drilled every 7.62-cm along the length on both sides of the mold to allow the two halves to be bolted together. An opening was also cut through one of the end caps. This allowed for the AFC wiring to be passed to the outside of the mold during cure.

The wires were wrapped in non-porous teflon. This ensured that no excess resin would coat the wires. Fabrication of the wing mold was carried out at the MIT Central Machine Shop.

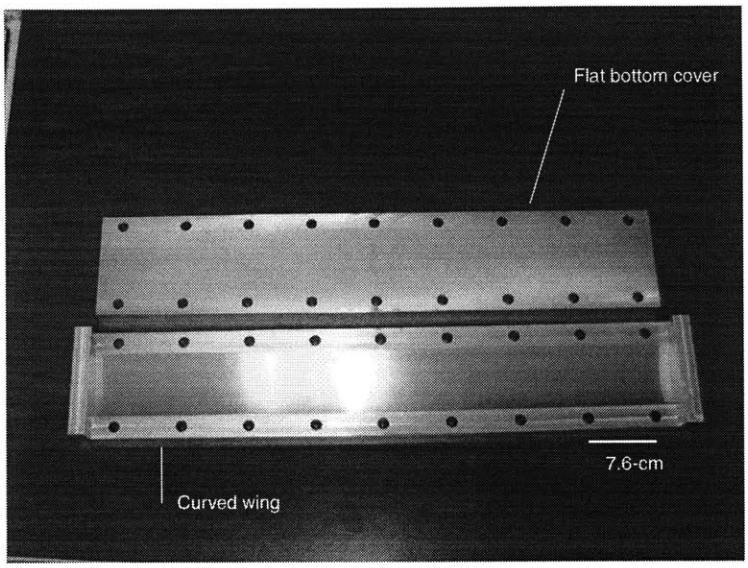


Figure 4-1: Wing mold

4.2 Foam Cores

The cores of the wings consisted of Rohacell 31 foam. The core was shaped to provide back pressure for the surrounding composite during the cure. The foam cores for the wing needed to be machined to the aerodynamic shape of the airfoil. As a base point, the shape of the mold was used. The ply and AFC thicknesses were then subtracted from this shape. An additional 0.254-mm to 0.381-mm was then added to the thickness of the foam cores. This was done in order to provide sufficient back pressure on the composite laminates during the cure cycle, ensuring the correct outer mold lines. Due to the high temperature properties of Rohacell, a hot wire cutter could not be used for fabrication. Once the correct shape was calculated for the cores, the drawing was imported into Mastercam in order to generate a tool path. The foam cores were then machined in 40.6-cm segments on a 3-axis CNC milling machine. An example of the final product is shown in Figure 4-2.

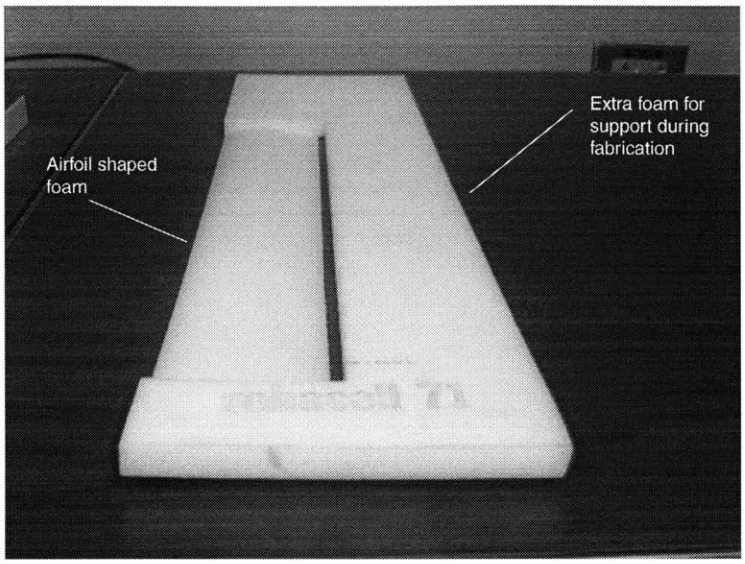


Figure 4-2: Foam core

4.3 Active Elements

4.3.1 Flexible Circuit

A flexible circuit was required in order to achieve a low volume/low profile solution to the challenge of distributing power to the AFC packs. The circuit consists of multiple parallel lines of wiring embedded in a thermoplastic material with an insulating cover of kapton. The gauge of the wires was selected based on the smallest possible diameter capable of carrying the current required to drive the individual packs. A 34-gauge magnet wire was chosen. This wire has a diameter of 0.1601 mm and has a normal current rating of 79.5 mA. The spacing of the individual wires was designed to ensure that the high voltages would not cause arcing between adjacent lines, resulting in a short circuit.

The outline of the the AFC patches was laid out on a board (Figure 4-3). Traces were then drawn to represent the wire spacing within the flexible circuit. For ease of fabrication, the wires were spaced 0.3175 cm (0.125") apart. This distance is well above the required spacing based on the dielectric strength of the thermoplastic (120,000 V/mm). A sheet of 0.127 mm Ultem was then placed on the board and secured with nails. The nails provided a guide for placing the individual wires within the circuit. Once all six lines were laid out

and pulled tight, they were secured using kapton tape. The purpose of the tape was twofold. It provided a means of securing the lines and ensuring that they remained parallel along the length of the circuit. The tape also provided an additional layer of electrical insulation. This would help to ensure that the circuit would not fail by arcing through the thickness of the thermoplastic and travelling through the conductive carbon on either side. The circuit was then flipped over, and an additional layer of Ultem and kapton tape were applied. This additional layer of Ultem provides sufficient thickness so that the wires end up completely embedded in the thermoplastic.

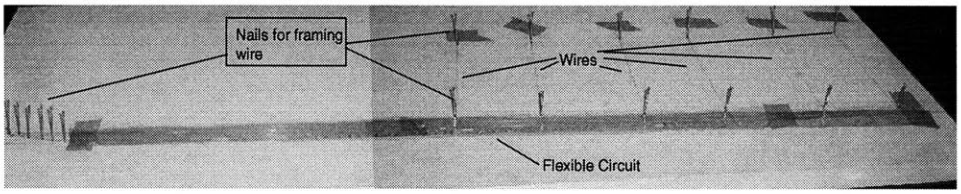


Figure 4-3: Flexible circuit template

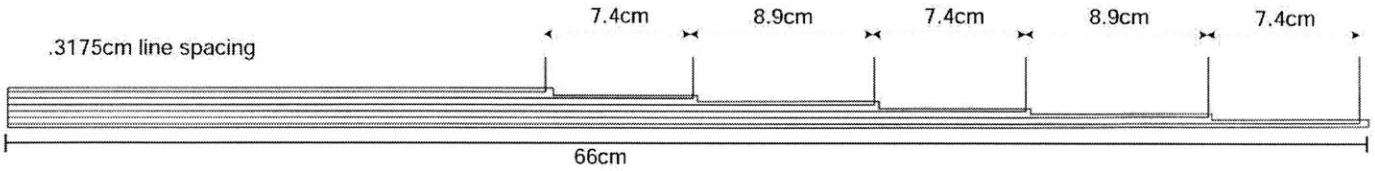


Figure 4-4: Flexible circuit drawing

This fabrication technique was carried out using a small scale specimen. The specimens were laid out and fabricated using a hot press. Once the circuit was cured, it was sandwiched between two pieces of carbon and cured using the identical cycle that would be applied to the wings. The circuit was then tested by applying a voltage across adjacent lines until they failed. Failure occurred at 4.9 kV. This is well above the operational limits expected.

The full scale circuits were then placed on a flat cure plate and sealed. The autoclave was required for the full scale because of the relatively small size of the hot press (35.6-mm x 35.6-mm). The high glass transition temperature of the thermoplastic (221°C) necessitated the use of non-porous teflon film instead of conventional vacuum bagging. Once sealed, the layup was placed in the autoclave and heated until the temperature of the plates reached

232°C. Once this temperature was reached, 206.8 kPa of pressure was applied to ensure that the two Ultem sheets were joined and that the wires were completely embedded.

4.3.2 Assembly

The circuits were then tested to ensure that they could provide the necessary power to the AFC patches without failure. Individual lines were hooked up to a power supply and a voltage of 4 kV applied. Once the circuits were tested, the AFC patches were laid out and the circuits connected. A final capacitance measurement was taken and compared with the results provided by the manufacturer: Continuum Control Corp., Billerica, Massachusetts. The results are summarized in Table 4.1.

Table 4.1: Actuator capacitance measurements

Serial #	From manufacturer (nF)	Measured (nF)	location
S/N 001	7.98	8.23	Lower surface root
S/N 003	7.48	7.62	Upper surface root
S/N 004	8.48	8.67	Upper surface mid
S/N 005	8.49	8.57	Upper surface tip
S/N 007	9.16	9.37	Lower surface mid
S/N 008	9.16	9.24	Upper surface tip

The lengths of the individual leads on both the circuit as well as the AFC were trimmed to eliminate any excess. The circuit leads were then soldered to the tabs on the individual AFC actuators.

The electrical connections between the circuit and AFC patches were then mechanically isolated from the surrounding carbon. The solder joint was sandwiched between two pieces of kapton tape to electrically insulate the joint. In order to ensure that this configuration would sustain the applied electrical loads, voltage was applied to a wire sandwiched between grounded aluminum plates with kapton tape as a barrier. The voltage was steadily increased until the dielectric breakdown occurred at approximately 5 kV.

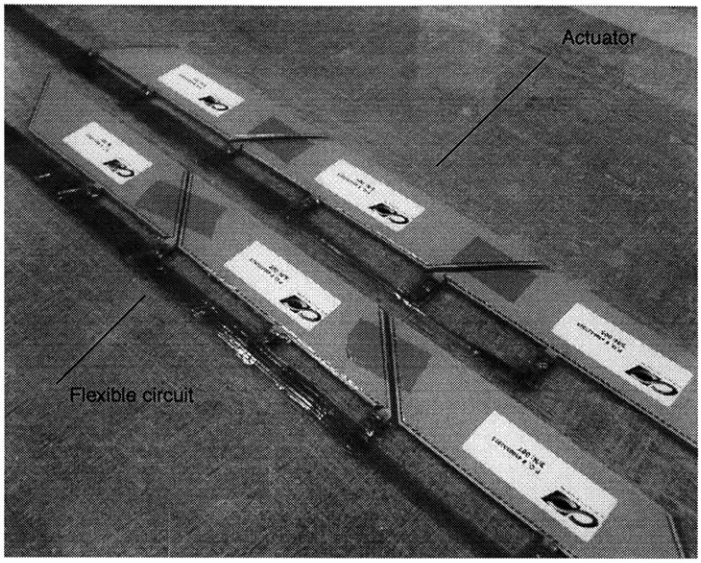


Figure 4-5: Circuit and actuators

4.4 Final Assembly

In preparation for curing, all surfaces of the blade mold were cleaned. Excess resin from previous cures was removed and the mold was coated with five coats of mold release. The releasing agent used was not in aerosol, but rather in liquid form. This prevents any pock-marks developing on the surface of the foil that may result from condensation of water on the surface of the mold.

Prior to assembly, the Rohacell foam cores were heated to 266°F for 24 hours. This was done to remove any moisture that may have been absorbed into the foam. Moisture has a plasticizer effect on Rohacell. The addition of moisture may result in loss of compressive strength as well as wrinkling of the foam cores.

Two sheets of AS4/3501-6 pre-preg were then cut. The dimensions of the sheet are 0.66 m x 0.1486 m with the 0° aligned with the long axis of the piece. The length of the outer contour of the airfoil was calculated using a MATLAB script (Appendix B). The first sheet of pre-preg is then laid out, aligning the edge of the material with the trailing edge of the foil. The material is then laid out along the curved surface of the mold. The AFC and the attached circuit are then laid in place, and the second sheet applied. At this stage, the foam cores are added and the innermost ply of pre-preg was wrapped around them. This ensures

that the leading edge of the wing is continuous. The second AFC group with the attached circuit is then laid out and the outer layer of carbon is wrapped around. The wiring for the circuits is passed through the end cap, and the mold is then closed and bolted. Pressure is applied to the mold to ensure the two halves are uniformly spaced. The fabrication steps are illustrated in Figures 4-6 through 4-10

The mold was then placed in the postcure oven and heated to 315°F. This lower temperature was required to ensure that the Rohacell cores did not exceed the heat deformation temperature. In order to ensure that the wing would be sufficiently cured, the mold was left at temperature for 3 hours. At the end of 3 hours, heat was removed and the oven was cooled at a rate of 5°/minute. This serves to avoid thermal shock in the composite which may produce cracks.

Once the wing was removed it was visually inspected to determine if the cure was successful. Initial observations showed a good surface finish over a majority of the wing. However, certain regions appeared to be low in resin content. In particular, these regions occurred surrounding the AFC packs, with the most severe instances occurring at the leading edge. A wrinkle in the surface finish was also detected at the leading edge. This wrinkle could be easily filled with epoxy, and consequently should not adversely affect the aerodynamic performance of the wing. The asymmetric location of the AFC packs also induced a pretwist in the wing. The pretwist tip angle was measured to be approximately 5.22°. These are shown in Figure 4-11.

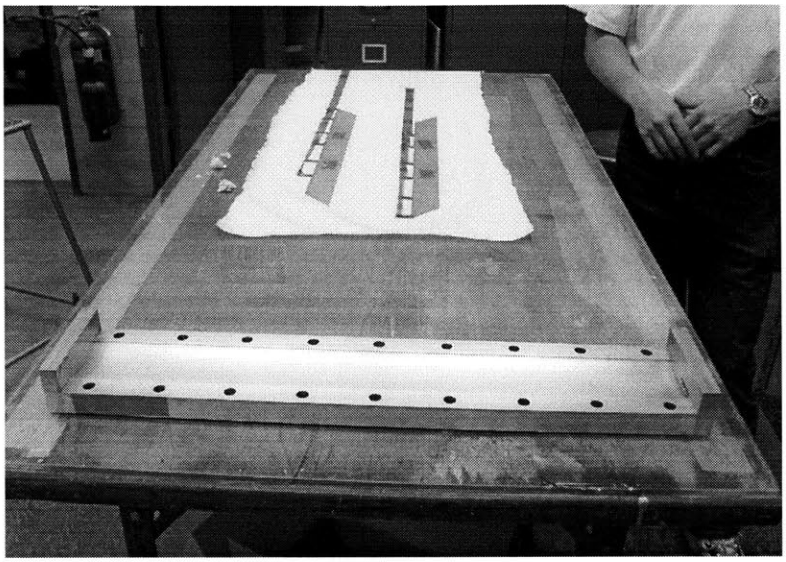


Figure 4-6: Wing mold and actuators

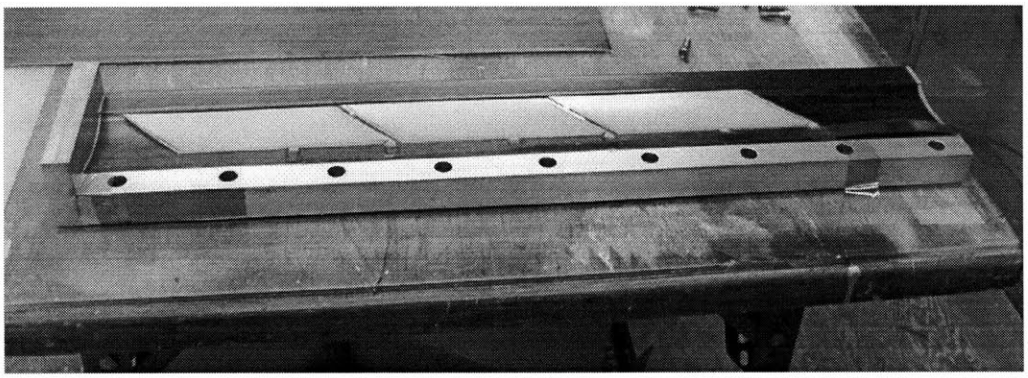


Figure 4-7: Outer ply and upper surface actuators

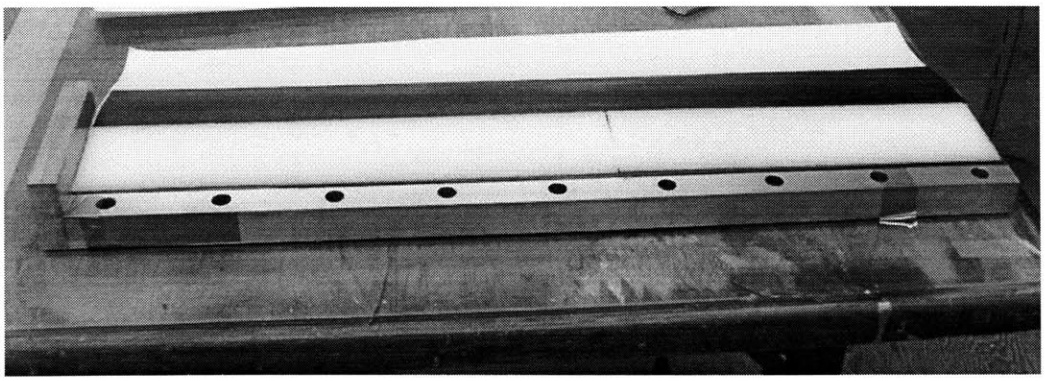


Figure 4-8: 2 composite plies and foam cores prior to folding

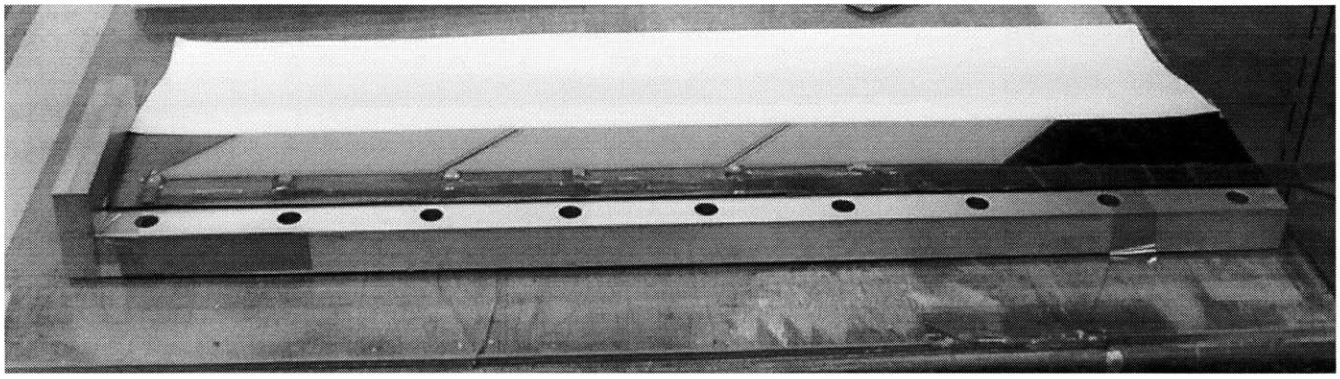


Figure 4-9: Lower surface actuators

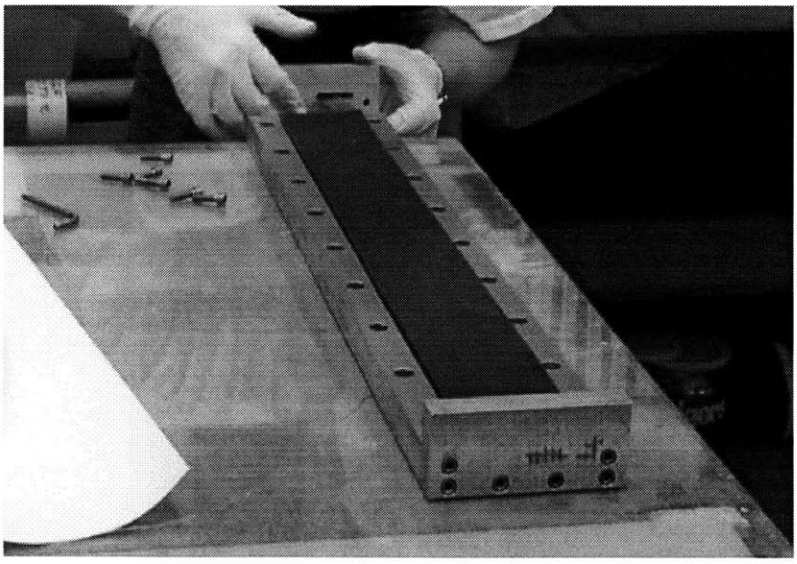


Figure 4-10: Wing prior to closing of the mold

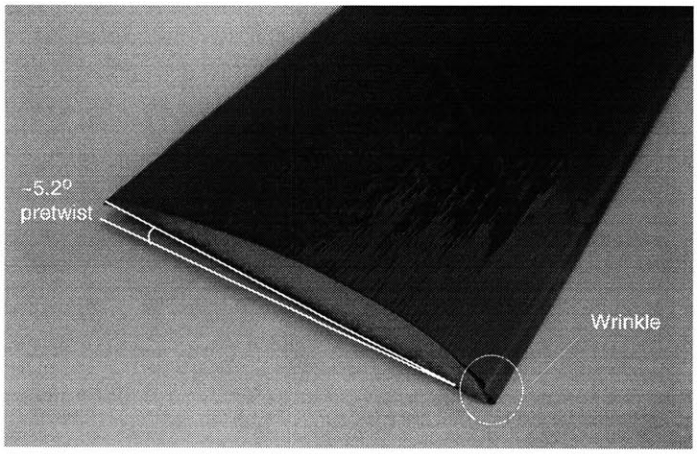


Figure 4-11: WASP wing tip after fabrication

Chapter 5

Testing and Results

Following fabrication, the wing was bench tested to determine whether the actuators had survived the fabrication process. The wing was further characterized to determine the voltage twist transfer function as well as the natural frequencies and operating limits of the wing.

5.1 Bench Testing

The WASP wing was placed on a bench and tested. Initially, admittance measurements were carried out on the individual packs in order to determine whether the actuators were still functional after the fabrication process. Once this was done, the wing was mounted in an aluminum clamp (Figure 5-2) and secured to a vibration isolation table. The wing was then treated with a paint spray to ensure good reflectivity for the laser displacement sensors. A Polytec scanning laser vibrometer, model # PSV-300 with a OFV-056 optical scanning unit (Figure 5-1), was used to calculate the out of plane displacements of the wing tip. These measurements were then used to calculate the wing tip twist.

A sinusoidal waveform was input at a range of frequencies in order to calculate the frequency response of the wing as well as the normal modes. A waveform of 500 V p-p was input and the frequency gradually increased from 1 through 200 Hz in 5 Hz increments. The value of this increment was reduced around the expected resonance peaks. This was done in order to measure more precisely the resonant frequencies. The waveform was also used to



Figure 5-1: Laser vibrometer

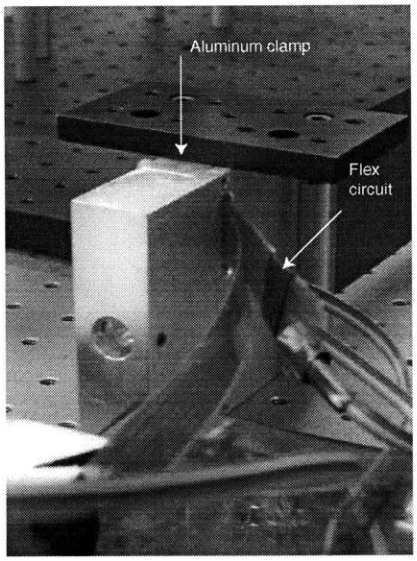


Figure 5-2: Aluminum clamp

calculate the voltage twist transfer function of the wing. Values for the linear displacement of the two points at the tip of the wing were correlated with the varying amplitude values over the range of the input waveform. These displacements were then used to calculate the twist angle at the tip of the wing using the following relation:

$$\theta = \arctan\left(\frac{d_1 - d_2}{L}\right) \tag{5.1}$$

Where d_1 and d_2 are the displacements of the two points and L is the chordwise distance between them (Figures 5-3 and 5-4).

The vibrometer typically is used to determine the vibration of a structure by measuring

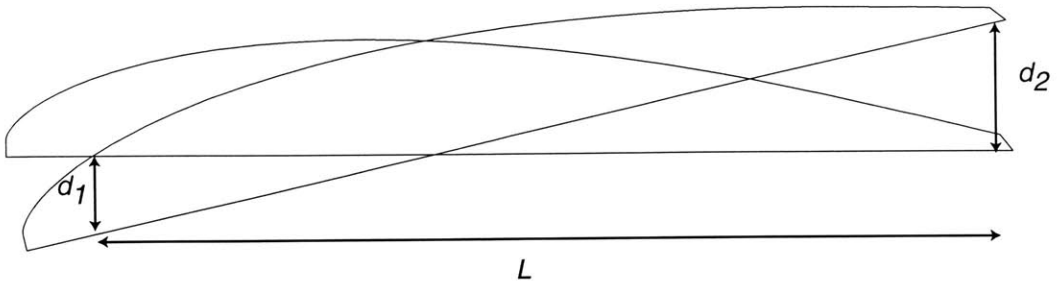


Figure 5-3: Displacement sensor measurement

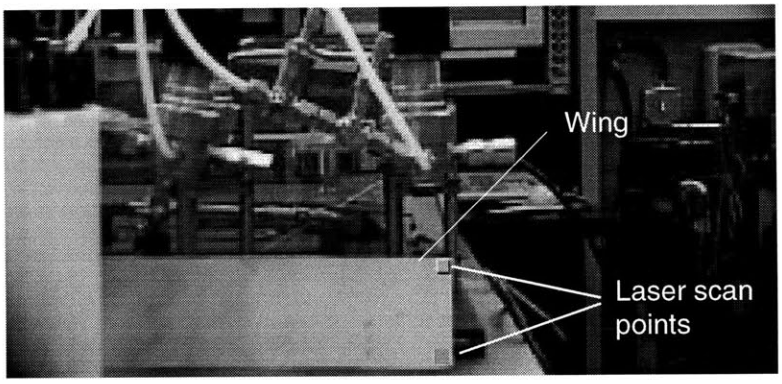


Figure 5-4: Displacement sensor setup

the velocities of sets of points. In order to calculate displacements, the software integrates the velocity over a time step. This method leads to the accumulation of error within the displacement measurements. This error would accumulate given a multiple point scan on the surface of the wing. In order to avoid this, the displacement measurements were taken at individual points over a 4 second interval. This minimizes the integration error while still capturing several actuation cycles on the wing. The input signal was recorded along with the magnitude and phase of the response of the wing. Using the magnitude and phase of the displacement allows for the displacement values to be shifted along the time scale of the input signal. This ensures that the displacements of the two points are applied to Equation 5.1 at the same relative point in time.

Once this characterization was done, the wing was tested at several higher voltage points. This was done to simulate the operating voltages expected. A sinusoidal waveform of 2000 V p-p was input with 0 V DC offset. The frequency was varied from 0.1 through 1, 5, and 10 Hz.

5.2 Results

Initial bench top testing confirmed that the individual AFC packs had survived the fabrication process. Admittance measurements indicated the presence of working active material within the individual circuit lines.

5.2.1 Actuator Free Strain Characterization

An AFC pack from a different batch was characterized on the bench in order to determine the free strain behavior of the actuator over a range of input voltages at frequencies of 0.5 and 5 Hz (Figure 5-5).

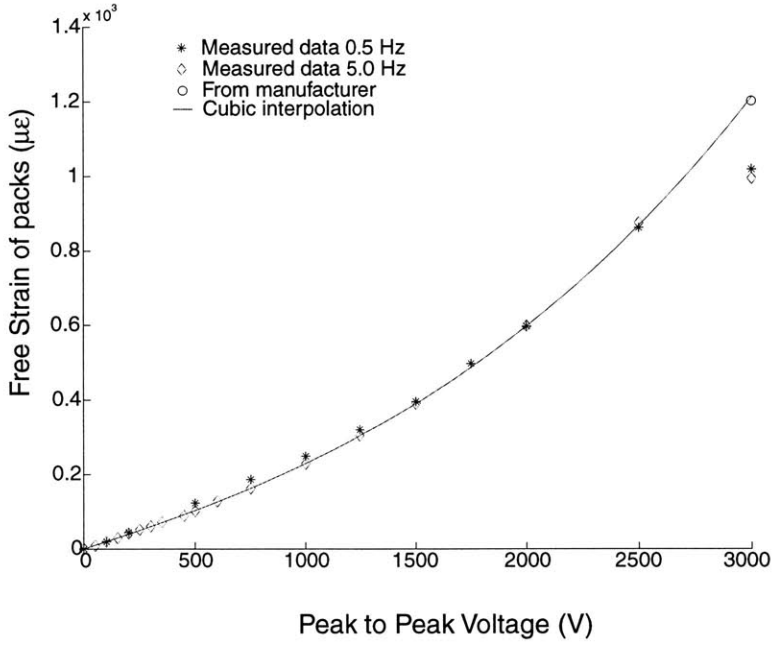


Figure 5-5: Free strain of actuators

The test setup involved placing the actuator on a teflon coated platform. One end of the AFC was clamped while the other was connected to a small teflon coated mirror. The displacement of the mirror was recorded using a laser sensor and the corresponding displacements were resolved into strain values. In order to ensure good reflectivity from the laser, a small weight was placed on top of the mirror. This served to ensure that the mirror did not deflect out of plane as a result of the pack actuation. At higher actuation

loads, additional weight was required to maintain the position of the mirror. The lower than expected value of the free strain at 3000 V p-p was due to this additional weight. The additional force of the added weight serves as a constraint on the displacement of the actuator. This results in a loss of measured actuation. Plotting the expected strain value at this voltage provided from the manufacturer results in good correlation to the trend.

5.2.2 Twist Actuation

The actuator packs (Figure 5-6) were connected to a Hewlett Packard 33120 15 MHz multifunction signal generator and a Trek 663A HV 1000x amplifier. An attenuator was used to ensure that the actuators would not be exposed to a voltage spike when the amplifier is engaged or the input signal adjusted. A sinusoidal waveform was input and the voltage increased.

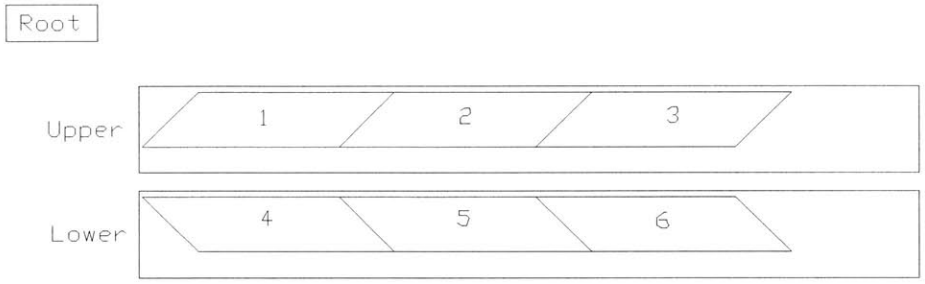


Figure 5-6: Actuator pack numbering scheme

Immediately the current limiter on the amplifier engaged revealing the presence of a short in the system. Capacitance measurements were then conducted on the individual packs to determine whether the AFC or the circuitry was damaged. Initial measurements revealed an infinite capacitance for pack 3. A finite value for the resistance was also measured for this pack (262 Ω). These values indicate the presence of a closed circuit implying a failure in the AFC pack itself.

Pack 3 was eliminated from the circuit and a voltage of 350 V p-p was applied. Immediately, the current limiter engaged indicating the presence of another short. In addition, audible popping was heard where the voltage was arcing through the conductive material of the wing. Unlike the previous case, the behavior of the current limiter was periodic indicating

that the individual pack could sustain a very low voltage before arcing through the material. The wing was disconnected from the power supply and capacitance measurements carried out on all the packs. The capacitance measurements on the remaining packs were finite with the resistances being infinite. The finite values for the capacitance and the infinite values for the resistance demonstrate that the circuits were open. This supports the conclusion that there were no shorts in the remaining actuators. The packs were powered up again individually with the current limiter engaging with pack 2. This confirmed the location of the short. The wing was powered up again without packs 2 and 3 with no shorts being recorded. In this case, the finite capacitance of the pack along with the infinite resistance lend themselves to the conclusion that the electrical failure occurred within the flex circuit or the connections and not within the individual pack itself. These results are summarized in Table 5.1.

Table 5.1: Capacitance and resistance measurements for first failed packs

Pack	Capacitance (nF)	Resistance
3	∞	262 Ω
2	12.05	∞

The remaining packs were then powered with a sinusoidal waveform at 5 Hz and 350 V p-p amplitude. The laser vibrometer was then set and displacement measurements were conducted at the leading and trailing edge of the wing tip. These measurements are shown in Figure 5-7. The output of the vibrometer along with the input signal was recorded using an oscilloscope interface in Labview. The response to the wing was sinusoidal and was in phase with the input signal as expected. A peak to peak twist angle of 0.138° was measured (Figure 5-8).

A finite element model was constructed in NASTRAN to model the measured data for the four-pack configuration. The free strain value for the actuators at 350 V p-p was input into the model. Analysis from NASTRAN predicted a peak to peak tip twist angle of 0.1475°. This corresponds to an error of 6.9%. Table 5.2 summarizes these results.

The slight over prediction of the twist value is due to the fact that the free strain of the

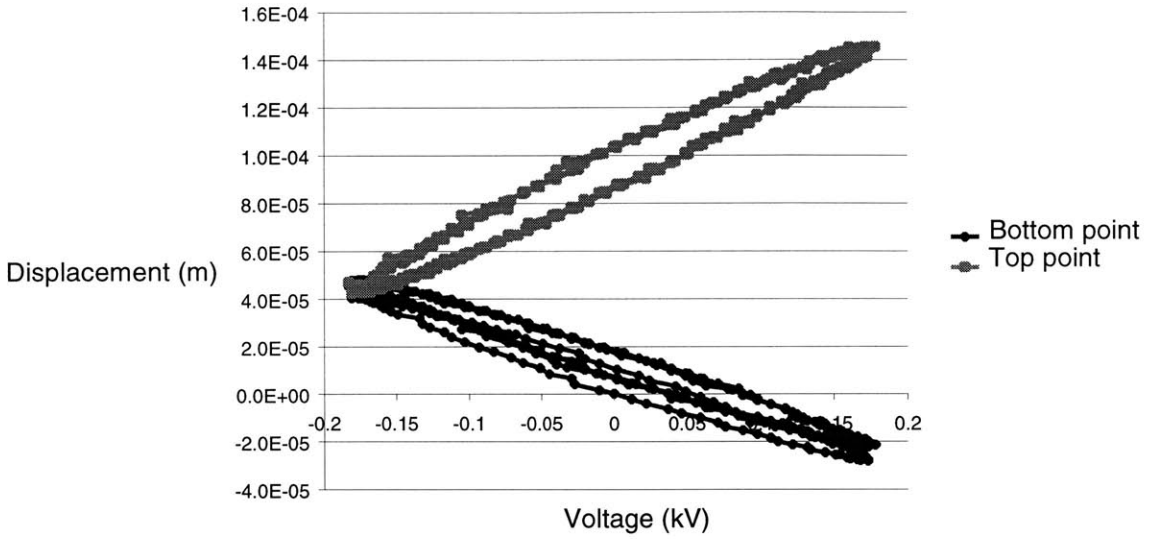


Figure 5-7: Vibrometer displacement measurements of active wing excited at 350 V p-p/5 Hz

Table 5.2: NASTRAN correlation

Measured	NASTRAN	% error
0.138°	0.1475°	6.9 %

AFC packs was used. Work done by Schmidt [25] has shown that lamination as well as heating of AFC packs may result in a degradation of the strain values. This degradation is due to constraint on the deformation of the actuators as well as the mismatch between the modulus of the AFC and the surrounding laminate.

The voltage on the wing was then increased to 500 V p-p. The wing responded and no additional short circuits were detected. After approximately 15 minutes of actuation, an audible pop was heard. Inspection of the amplifier indicated that the current limiter had engaged. The packs were disconnected from the wing and capacitance and resistance measurements conducted. All the remaining packs had an infinite resistance with finite capacitance values, indicating that there was not a failure within the actuators. Individual actuators were reconnected to the wing to determine the location of the short. Immediately

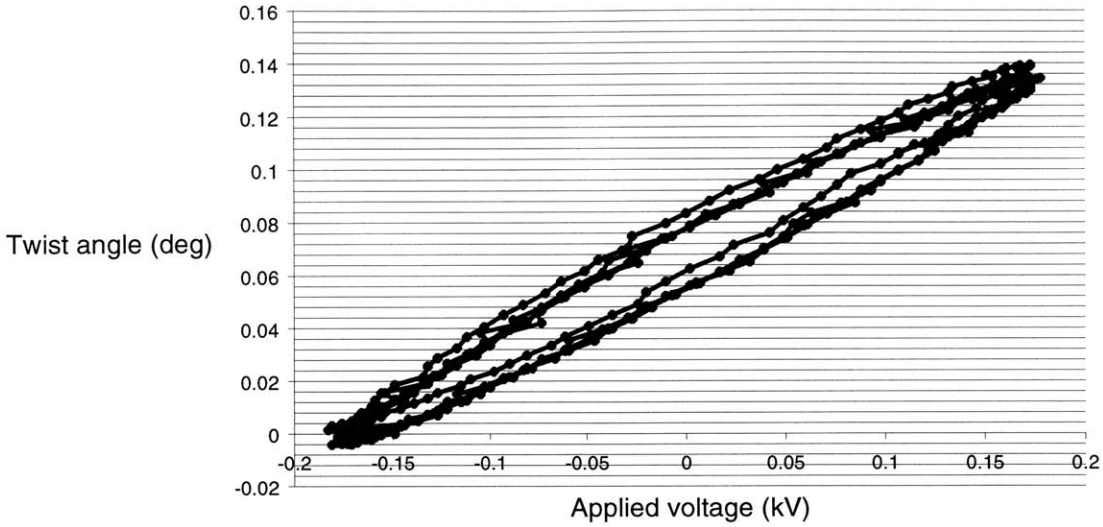


Figure 5-8: Voltage-twist relationship at 5 Hz

after connection of pack 6, a loud periodic popping sound was heard as the voltage was arcing through the composite structure. This was further confirmed by the current limiter. Pack 4 was then connected to the amplifier and the voltage gradually increased. The actuator was able to sustain very low voltages, however the current limiter engaged well short of the 500 V p-p target. As before, the behavior of the limiter was periodic indicating the actuators could not sustain voltages over the higher amplitude portions of the cycle.

5.2.3 Resonance Frequency Characterization

The laser vibrometer was then used to calculate the normal modes of the wing as well as the frequency response. The remaining two actuators were excited with a 50 V p-p sine chirp over a frequency spectrum of 1 to 200 Hz. The displacement of two points (Figure 5-4) at the tip were measured as well as the relative phase of the displacement to the input signal. A fast fourier transform of the displacement was taken and the results plotted in Figure 5-9. The first bending and torsion modes of the wing were captured and were compared to the values predicted from NASTRAN (Table 5.3). In addition, the second bending mode of the

wing is captured.

Table 5.3: Frequency response of wing

Mode	NASTRAN	Experiment
First Bending	27 Hz	21 Hz
First Torsion	171 Hz	162 Hz
Second Bending	148 Hz	128 Hz

The difference of the measured response to the model predictions was a result of variations between the experimental and theoretical boundary conditions. The model assumed a rigid clamp boundary condition. However, the aluminum clamp was initially machined slightly larger than the airfoil section. This was done to ensure that the wing as well as the active elements embedded in the composite would not be crushed when the clamp was closed. The additional space in the clamp was filled using plastic shim stock. The addition of this shimming material ensured a snug fit in the clamp. However, the boundary condition was not ideally rigid.

The individual modes were identified by the phase angle of the displacements to the input signal. The phase difference in the response of the two points was used to calculate their relative displacement. A phase difference of 180° indicates that the points are moving in opposite directions. This results in a twist deflection of the wing. Conversely, a 0° or 360° phase shift indicates the points are moving in the same direction at the same instant in time. This corresponds to a predominately bending motion at the wing tip.

5.2.4 Powering to Design Conditions

The remaining two actuators were then connected to the power supply and the voltage steadily increased up to the expected operating voltage of 2000 V p-p. The actuators were connected separately and the voltage and twist measurements recorded. Two Keyence LB-72 laser sensors were used to measure the displacement of the two points simultaneously. This setup is depicted in Figure 5-10.

Actuator 1 was connected to the amplifier and a 0.5 Hz signal with no DC offset was

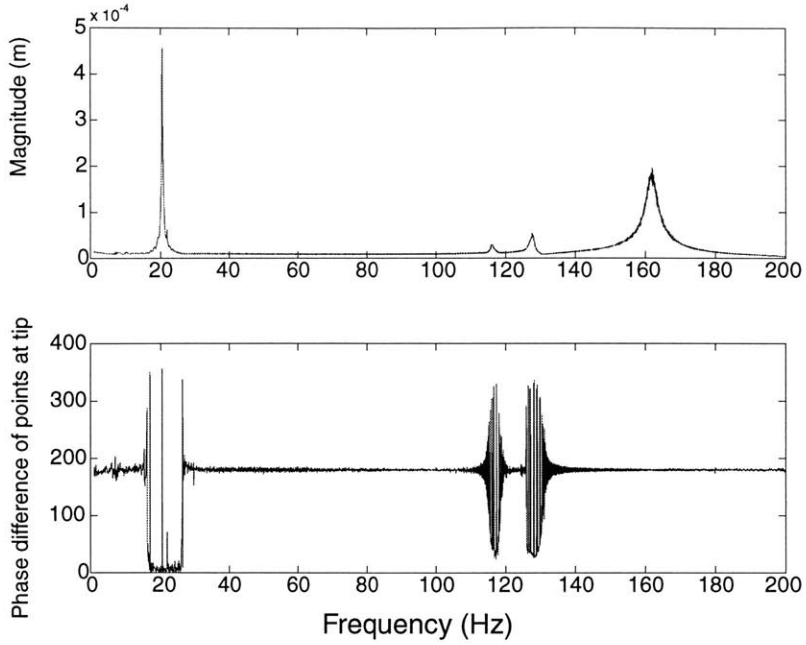


Figure 5-9: Frequency response of wing

steadily increased from 200 V p-p. The actuator successfully reached the operating voltage of 2000 V p-p without failure. The voltage twist relationship of the wing is shown in Figure 5-11. The resultant configuration was modelled in NASTRAN and errors between 30% and 40% were determined with respect to the measured data (Table 5.4).

Actuator 5 was then connected to the amplifier and the voltage steadily increased. The actuator successfully sustained voltages up to 1350 V p-p. After approximately one minute of actuation at this voltage an audible pop was heard indicating a short. This was confirmed by the current limiter on the amplifier. Capacitance and resistance measurements indicated a possible failure in the circuitry. However, unlike previous failures, the circuit could not support any voltage at all. The twist response is shown in Figure 5-12. The configuration was modelled in NASTRAN and again errors between 30% and 40% were present. The slightly higher error in this configuration was the result of very small displacement values for one of the measured points on the wing. As a result, the measured values for the displacement at this point fell within the noise of the sensor.

To understand these discrepancies, consider the following. The twist angle at the tip of the wing comes as a result of a bend-twist coupling present in the wing. The asymmetric

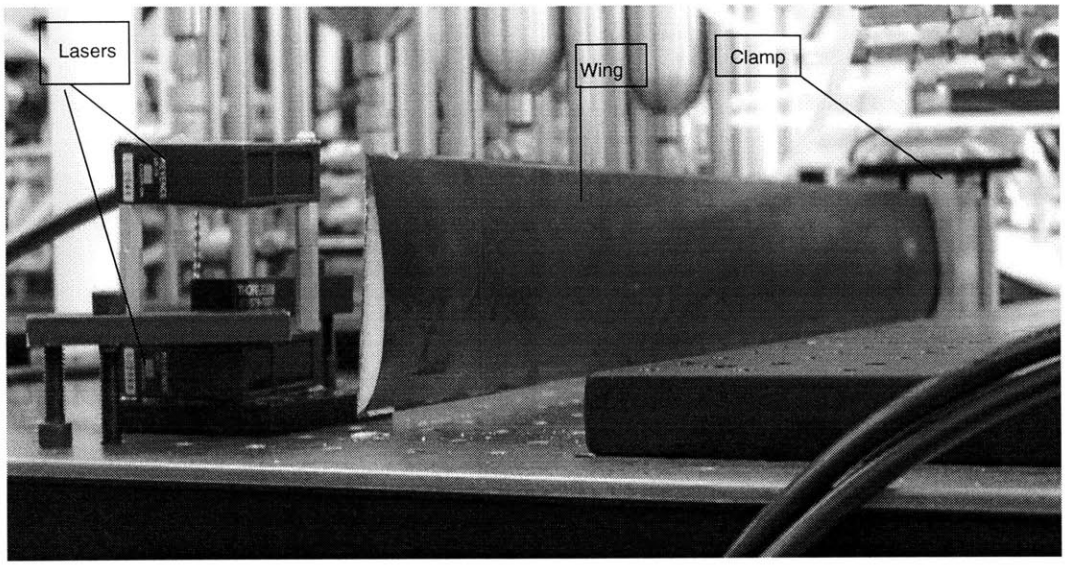


Figure 5-10: Laser displacement sensors setup

Table 5.4: AFC behavior- high voltage

Pack	Voltage	% error with model
1	2000 V p-p	30%-40%
5	1350 V p-p	30%-40%

chordwise layup due to the presence of the actuators as well as the asymmetric geometric section of the wing result in a net bending moment from a twist actuation. However, unlike a pure torsional actuation, as in the case of packs on the upper and lower surfaces of the wing, the resultant twist does not occur about the shear center of the wing. The net deformed shape may be described as a combination of this pure shear deformation coupled with a bending deformation. This has the effect of having the wing twist about the leading edge of the wing. This phenomenon was observed experimentally and confirmed in NASTRAN. Figure 5-13 shows the deformed shape of the wing from the model. This additional bending deflection causes the tip of the wing to move further out of plane. As a result, the laser displacement sensors measure higher values. In addition, the spanwise position of the lasers were offset by approximately 2 mm. This further magnifies the lasers capturing the non-twist deformations of the wing. These higher displacement values, when applied to Equation 5.1, result in higher than expected twist angles.

A final capacitance measurement was carried out on the wing and is summarized in Table 5.5. The presence of an insulating coat on the surface of the magnet wire resulted in inconsistent measurement of the capacitance post fabrication. This was remedied on testing when additional wires were soldered to the circuit. The high temperature of the solder serves to effectively remove the insulation from the wires. The additional wires were put in place in order to create a more robust connection to the amplifier.

Table 5.5: Final actuator capacitance measurements

capacitance (nF)	Pack #
9.35	1
12.05	2
Failed	3
12.44	4
11.57	5
13.60	6

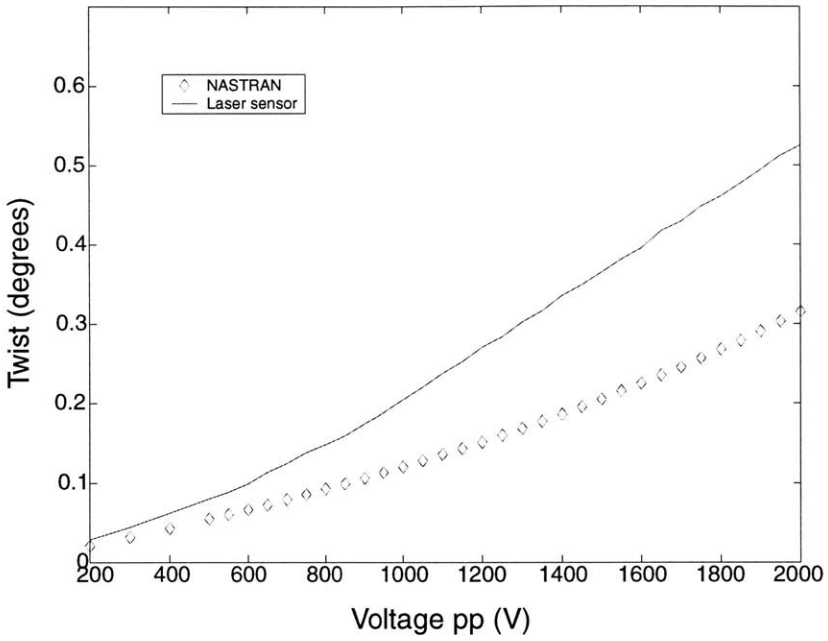


Figure 5-11: High voltage response of wing at 0.5 Hz (actuator 1 only)

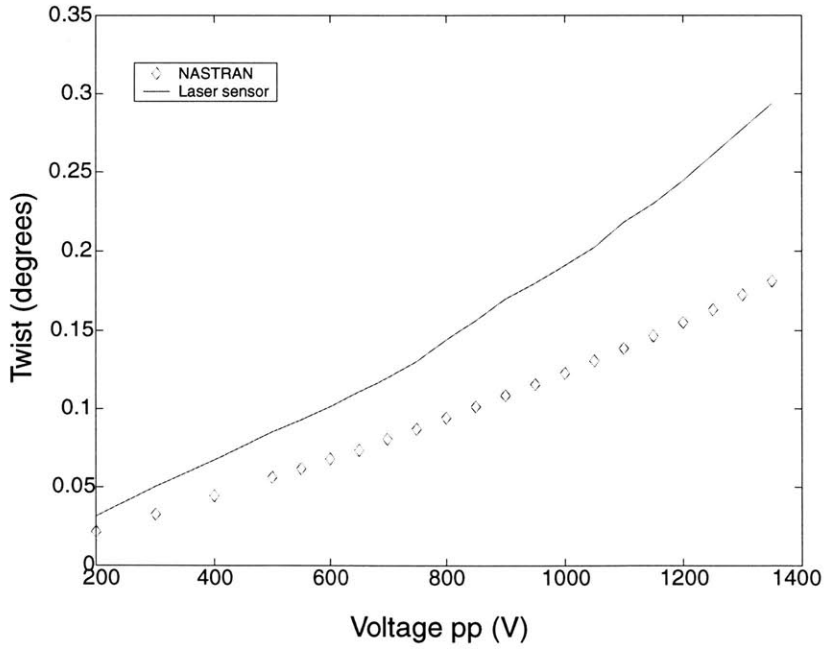


Figure 5-12: High voltage response of wing at 0.5 Hz (actuator 5 only)

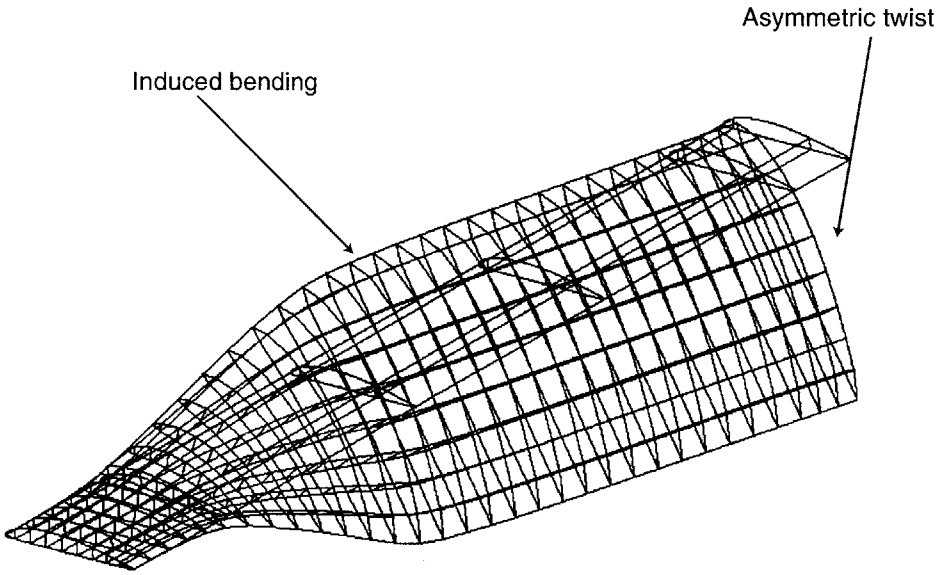


Figure 5-13: Deformed shape of wing (one actuator only)

Chapter 6

Conclusions

6.1 Summary

This thesis studied roll control concepts for a WASP-class vehicle. Initially, the study focused on several conventional actuation schemes as well as a slotted spoiler concept. Each of these candidate configurations were examined and evaluated based on cost, weight, and mechanical complexity. From this comparison, two viable configurations were identified and pursued. The first scheme involved the use of apertures to alter the lift distribution along the wing. This scheme was experimentally validated and demonstrated potential for success, however the lack of current actuator technology prohibited the fabrication of an active wing. The second actuation scheme, which became the main focus of this thesis, involved altering the lift distribution by warping the geometry of the wing. This was accomplished using embedded AFC actuators. These actuators offer the benefits of a savings in weight, mechanical complexity, as well as g-hardening. Aerodynamic, structural and aeroelastic models of this configuration were constructed. These models were validated using experimental data and have also demonstrated sufficient agreement with other modelling tools. The modelling demonstrated the feasibility of AFC packs for generating roll control. In addition, these models established a numerical framework that may be used for future wing design for a small scale reconnaissance vehicle.

Once the models were validated, they were used to optimize the layup of the WASP

wing. The layup converged on, meets all the requirements for twist actuation, aerostability, as well as launch loading. The fabrication of this wing also presented an improvement over the previous multistep wet layup process, allowing for a one step fabrication process in an autoclave environment.

The second portion of this thesis focused on the fabrication of the active wing. A flexible circuit was manufactured in house using magnet wire embedded within a thermoplastic matrix. Six AFC packs were embedded within the carbon structure and successfully cured. Several defects in the fabrication were detected. These defects manifested themselves in the form of short circuits through four packs as a result of connections between the individual packs and the circuit. A fifth pack was also lost due to a short circuit in the pack itself.

The data collected using the laser vibrometer demonstrated good correlation with the model. The values predicted by the model resulted in a 7% error with the collected data. The NASTRAN model was also able to successfully calculate the natural frequencies of the wing. The discrepancies between the model and the experiment were a result of a non-fixed boundary condition in the experimental setup.

Finally, high voltage actuation tests were conducted. One pack was successfully raised to the operating voltage demonstrating the feasibilty of embedding an AFC pack within a conductive carbon wing. The measured data exhibited a 30% to 40% error with the NASTRAN predictions. This error was a result of the asymmetry of the wing as well as errors in the experimental setup.

This thesis has indicated that integral twist actuation can be used for controlling the roll rate of a small scale vehicle. However, several hurdles still exist with regards to the fabrication and insulation of these components within a conductive carbon structure. The finite element modelling determining the effects of the AFC actuators has also proven reliable.

6.2 Recommendations for Future Work

The implementation of AFC packs within a graphite composite structure requires strict tolerances in the layout and fabrication of the individual components. In particular, great care must be taken in the area of electrical connections. Resistance and capacitance measure-

ments have revealed that a hard short was not present in four out of the five actuators. Consequently, the flex circuit and connections appear to be the location of the short.

The reliability of the electrical connections may be improved in several ways. The small wires embedded in the flex circuit made fabrication of the circuit very difficult. The small gauge along with the relative long distance of the electrode leads made it difficult to maintain an even spacing along the length of the circuit. The wires were also spaced much farther apart than necessary. This was due to the difficulty in laying out even parallel leads below a certain spacing.

The implementation of a commercial grade flex circuit would help to alleviate these problems. These circuits are manufactured by etching copper clad kapton and sandwiching the circuit between a second kapton layer for electrical insulation. These circuits have the benefit of being able to maintain even distances over a long length with line spacing as small as 0.12 mm. Decreasing the spacing of the individual leads to the minimum required would result in a thinner circuit. This would facilitate the fabrication as the current circuit and pack geometry nearly exceeded the allowable width set by the geometry of the wing. The circuit leads may also be terminated in a variety of geometric shapes and connectors. This would facilitate the solder connection between the AFC packs and the flexible circuit. By terminating the leads in a square solder pad, the surface area of the solder connection could be increased, resulting in a more reliable bond. The low profile joint would also help in applying electrical insulation.

The electrical insulation of the solder connections also requires improvement. The insulation can be easily increased by moving to a thicker kapton tape surrounding the joint. The joint may also be potted in a non-conductive epoxy prior to the application of the kapton. This would serve as an additional layer of insulation as well as eliminate any possible voids that may exist with the application of kapton tape alone.

Moreover, modifying the geometries of the AFC packs may also benefit both the performance of the wing as well as the fabrication. The actuator packs chosen were selected based on availability. The packs were not optimized for the geometry of the wing used in this study. This resulted in approximately only 75% of the wing span being covered with actuators and approximately 60% of the chord. Decreasing the length of the actuators would

allow for the placement of a 4th actuator along the span. This would allow for the full span of the wing to be used in controlling its roll performance. By increasing the width of the packs, additional control authority would be realized resulting in increased tip twist angles and roll torques.

Further work should be done to validate the buckling as well as the aeroelastic modelling conducted on the wing. In addition, the final wing configuration should be modelled including the effects of the hinge on the aeroelastic and buckling performance.

The effect of impact damage on the wing may also need to be investigated. Placement of the AFC packs one layer from the surface of the composite may be insufficient in the prevention of damage due to foreign object impact. This may result in a loss of actuation due to damage of the pack as well as the electrical connections resulting in a loss of actuation and roll control.

The slotted wing concept presented in Appendix A has shown promise for implementing roll control in a small scale UAV. Further work should be done to optimize the layout as well as the geometry of the apertures. Currently, there is no sufficient actuation mechanism for this concept. Additional work should focus on the development and implementation of an appropriate actuation mechanism to fully take advantage of this concept.

Finally the power requirements and electronics volume for the AFC packs need to be addressed. Current off-the-shelf components offer the capability for high voltage amplification, however the smallest amplifiers may still be too large for the volume available in a WASP-like vehicle. In addition, for the WASP mission profile, any additional electronic components would need to be g-hardened.

Future work of the WASP wing studied in this thesis should focus on developing a repeatable robust method for using active fiber technology as means for implementing roll control. Work should focus on the implementation and connection of a flexible circuit within the structure of the wing and the possible effects of long term storage of the system.

Bibliography

[1] http://www.fas.org/irp/program/collect/uav.htm.

[2] Sean George, 2000. Draper Laboratory, private communication.

[3] Nikhil A. Koratkar and Inderjit Chopra. Design, fabrication and testing of a mach scaled rotor model with trailing edge flaps. *Annual Forum Proceedings American Helicopter Society v 55*, 1:558–578, May 25-27 1999.

[4] Steven R Hall and Eric F Prechtl. Develoment of a piezoelectric servoflap for helicopter rotor control. *Smart Materials and Structures*, 5(1):26–34, February 1996.

[5] Joseph W Clement, Diann Brei, Andrew J Moskalik, and Ron Barrett. Bench-top characterization of an active rotor blade flap system incorporating c-block actuators. *AIAA Technical Paper*, AIAA-98-2108:2857–2869, 1998.

[6] Dhananjay K Samak and Inderjit Chopra. Design of high force, high displacement actuators for helicopter rotors. *Smart Materials and Structures*, 5:58–67, August 1995.

[7] Aditi Chattopadhyay, Charles E. Seeley, and lori Mitchell. Design of a smart flap using polymeric c-block actuators and a hybrid optimization technique. *Smart Materials and Structures*, pages 134–144, 1997.

[8] Ramesh Chandra and Inderjit Chopra. Actuation of trailing edge flap in a wing model using a piezostack device. *AIAA Technical Paper*, AIAA-97-1195:1438–1448, 1997.

[9] Razvan Rusovici and Harley H. Cudney. Design study of an adaptive, split-flap actuator. *AIAA Technical Paper*, AIAA-97-1080:203–212, 1997.

[10] Taeoh Lee and Inderjit Chopra. Development and validation of a refined piezostack-actuated trailing edge flap actuator for a helicopter rotor. *Smart Structures and Materials*, Smart Structures and Integrated Sysytems(1):22–36, June 1999.

[11] Eric F. Prechtl and Steven R. Hall. Design of a high efficiency discrete servo-flap actuator for helicopter rotor control. *Proceedings of SPIE the International Society for Optical Enginnering*, 3041:158–181, 1997.

[12] Steven R. Hall, Theodora Tzianetopoulou, Friedrich Straub, and Hieu Ngo. Design and testing of a double x-frame piezoelectric actuator. *Proceedings of SPIE the International Society for Optical Engineering*, 3985:26–37, 2000.

[13] Mark Drela, 2001. MIT, private communication.

[14] Andreas P.F. Bernhard and Inderjit Chopra. Mach-scale design of a rotor-model with active blade tips. *Annual Forum Proceedings American Helicopter Society v 55*, 1:579–598, May 25-27 1999.

[15] Kenneth B. Lazarus, Edward F. Crawley, and Charrissa Y. Lin. Multivariable active lifting surface control using strain actuation": Analytical and experimental results. *Journal of Aircraft*, 34(3):313–321, June 1997.

[16] Edward F. Crawley and Kenneth B. Lazarus. Induced strain actuation of isotropic and anisotropic plates. *AIAA Journal*, 29(6):944–951, 1990.

[17] Changho Nam and Youdan Kim. Optimal design of composite lifting surfaces for flutter suppression with piezoelectric actuators. *AIAA Journal*, 33(10):1897–1904, October 1995.

[18] Steven M. Ehlers and Terrence A. Weisshaar. Static aeroelastic control of an adaptive lifting surface. *Journal of Aircraft*, 30(4):534–676, July-August 1993.

[19] Aaron A. Bent and Nesbitt W. Hagood. Piezoelectric fiber composites with interdigitated electrodes. *Journal of Intelligent Material Systems and Structures*, 8(11):903–919, November 1997.

[20] SangJoon Shin and Carlos E. S. Cesnik. Design manufacturing and testing of an active twist rotor. Technical Report AMSL#99-3, Active Materials and Structres Lab, Massachusetts Institute of Technology, June 1999.

[21] Matthew L. Wilbur, Paul H. Mirick, William T. Yeager Jr., Chester W. Langston, Carlos E.S. Cesnik, and SangJoon Shin. Vibratory loads reduction testing or the NASA/Army/MIT active twist rotor. *Journal of the American Helicopter Society*, 57(2):1050–1069, 2001.

[22] Steven Hall, 2001. MIT, private communication.

[23] Mark Drela, last update 7 June 1994. AVL User Primer.

[24] Seth Kessler, 2000. MIT, private communication.

[25] Mads C. Schmidt Nesbitt W. Hagood IV. Development of integral actuation technology for composite rotorcraft structures. Technical Report AMSL#00-6, Active Materials and Structres Lab, Massachusetts Institute of Technology, December 2000.

[26] Viresh K Wickramasinghe Nesbitt W. Hagood IV. Characterization of active fiber composite actuators for helicopter rotor blade applications. Technical Report AMSL#01-02, Active Materials and Structres Lab, Massachusetts Institute of Technology, March 2001.

[27] Carlos E. S. Cesnik and Miguel Ortega-Morales. Active composite beam cross-sectional modeling stiffness and active force constants. *Proceedings of 40th Structures Structural Dynamics abd Materials Conference*, AIAA-99-1548, 1999.

Appendix A

Slotted Spoiler

Due to the difficulties in analyzing the aerodynamics of the slotted spoiler configuration, experiments were conducted to determine the feasibility of this means for roll control.

A.1 Fabrication

A baseline wing was obtained from Draper Laboratory. The wing was comprised of a foam core with the original baseline layup for the WASP wing. The geometric planform of the wing also corresponded to the original WASP design.

An array of 3 mm diameter holes was laid out with 1 cm spacing between adjacent actuators as shown in Figure A-1. This was done based on the assumption of a required support structure for the actuation technology. The apertures were placed such that the entire surface of the wing could be tested to determine the ideal location of the actuators. However, during the test runs no adjacent apertures were opened that were less than 1 cm apart. This allowed for the maximization of the test spectrum on the surface of the wing while still maintaining a minimum spacing between the individual holes.

Once the holes were laid out, they were cut through the thickness of the wing using an Omax water jet cutter. The combination of the cutting pressure as well as submerging the wing in water served to undercut the holes. This raised the concern that air would not be passing directly through the apertures as it would with real actuators, rather it would be

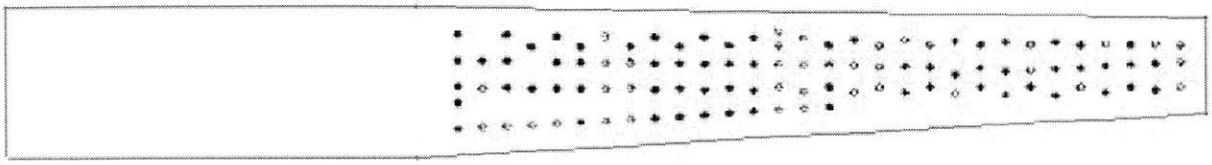


Figure A-1: Hole layout

diffusing through the core of the wing.

In order to alleviate this, the wing was submerged in a bath of hot wax. The benefits of this procedure was twofold. First it alleviated the problem of having the air diffuse through the voids in the core created by the cutting process. Secondly, it allowed for a convenient means for opening and closing the holes during the testing. The holes could now be easily opened manually by using a 3 mm drill bit and sealed by hand with a small amount of wax applied to both ends of the hole. Figure A-2 shows the final article.

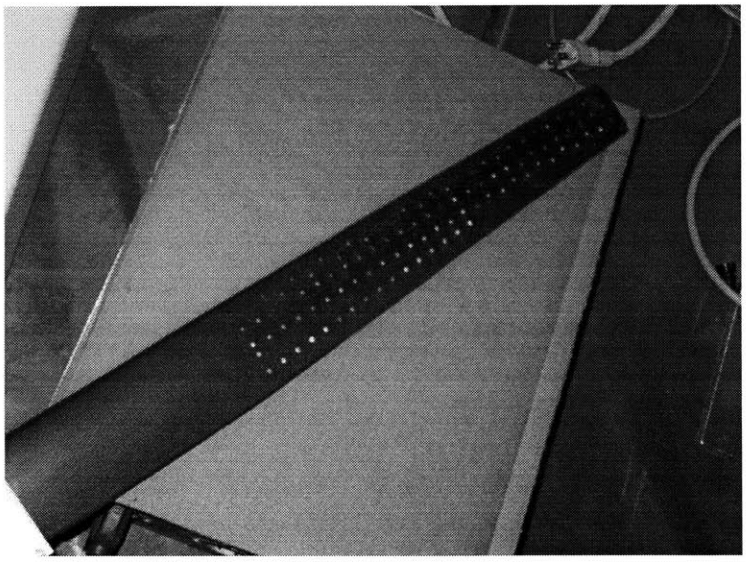


Figure A-2: Final wing with wax filled holes

A.2 Testing

The wing was mounted on a 110-N JR3 load cell and placed in the MIT Wright Brothers wind tunnel. The wing mount consisted of a modified version of the mount described in

Chapter 5 and it is shown in Figure A-3.

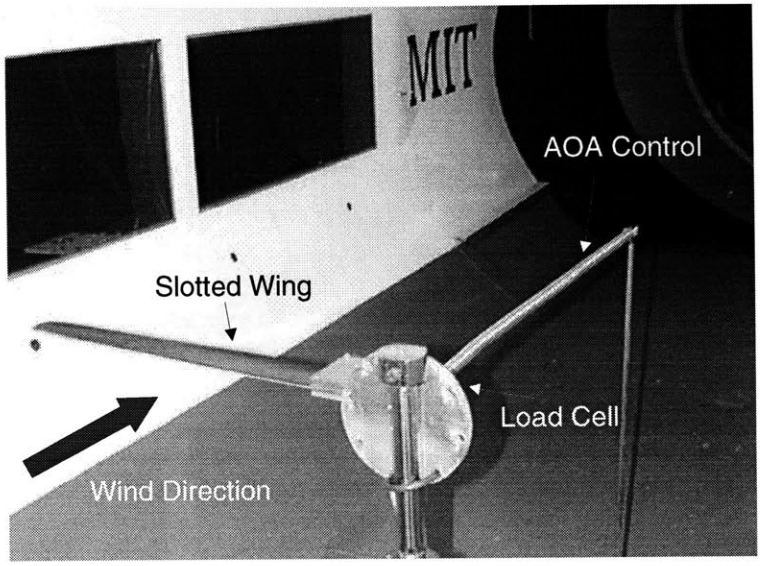


Figure A-3: Tunnel setup

The wing was tested at two operating points and through a variety of angles of attack. Individual holes were opened between runs in order to determine the effect of hole location on the roll performance of the wing. The test matrix is outlined in Table A.1.

Table A.1: Test matrix for the slotted wing (runs are at 18 m/s and 27 m/s)

Setting	A.O.A. (deg)										
	-4	-3	-2	-1	0	1	2	3	4	5	6
All Closed	2	2	2	2	2	2	2	2	2	2	2
Outboard L.E. open	2	2	2	2	2	2	2	2	2	2	2
Full L.E. Open	2	2	2	2	2	2	2	2	2	2	2
Full L.E. Outboard T.E.	2	2	2	2	2	2	2	2	2	2	2
Full L.E. and T.E.	2	2	2	2	2	2	2	2	2	2	2
Outboard L.E. and T.E.	2	2	2	2	2	2	2	2	2	2	2
Outboard Middle	2	2	2	2	2	2	2	2	2	2	2
Full Middle	2	2	2	2	2	2	2	2	2	2	2
All Closed	2	2	2	2	2	2	2	2	2	2	2

A.3 Results

Preliminary results indicated that the slotted spoiler concept was very effective in controlling the roll rate of the WASP vehicle. Figures A-4 and A-5 demonstrate how the presence of open holes in the wing are affecting the overall lift measured.

The measurement of roll torque shown in Figures A-6 and A-7 also demonstrate the effect of the holes on the roll moment. As expected, the behavior is linear with angle of attack. Note that the torque begins to level off with higher angles of attack for the baseline case. This was due to saturation of the load cell as the upper sensor limit was approached.

The net roll moment on the vehicle can be extracted by subtracting out the roll torque due to the baseline configuration with all the holes closed. This is shown in Figures A-8 and A-9, along with the baseline roll requirement

It is clear that net roll moment produced by the slotted configuration is well above the requirements. It was noticed, however, that there existed for different angles of attack some significant drift in the measured lift data compared to the two baseline cases: one measured at the beginning of the tests, and the second at the end. It is theorized that the drift occurred because of excessive temperature changes in the wind tunnel. An approximately 16.7° C rise in temperature was present between the first and last test run. This increase in temperature caused the wax within the wing to heat up and soften significantly. As a result, a noticeable dimpling effect occurred diminishing the smooth surface of the wing. For more accurate quantification of the results, a new set of tests must be conducted.

The slotted wing concept demonstrated significant potential for the implementation of roll control. It was decided, however, not to further pursue it in this current study since it requires the development of the actuator scheme that would control the flow through the holes. This is beyond the scope of the current study.

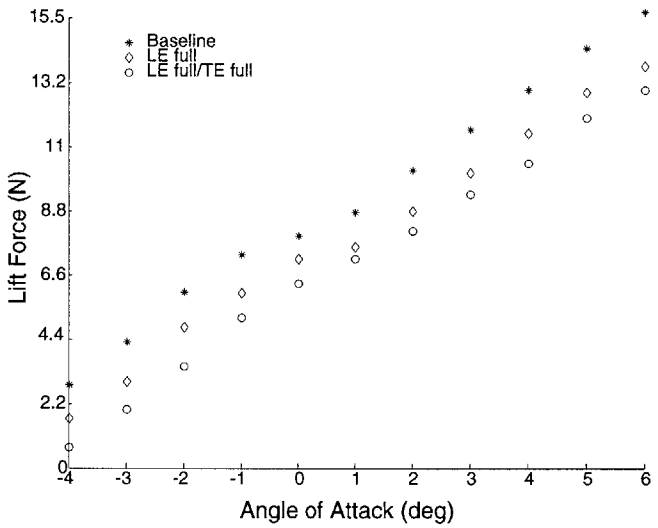


Figure A-4: Lift measurements at 27 m/s

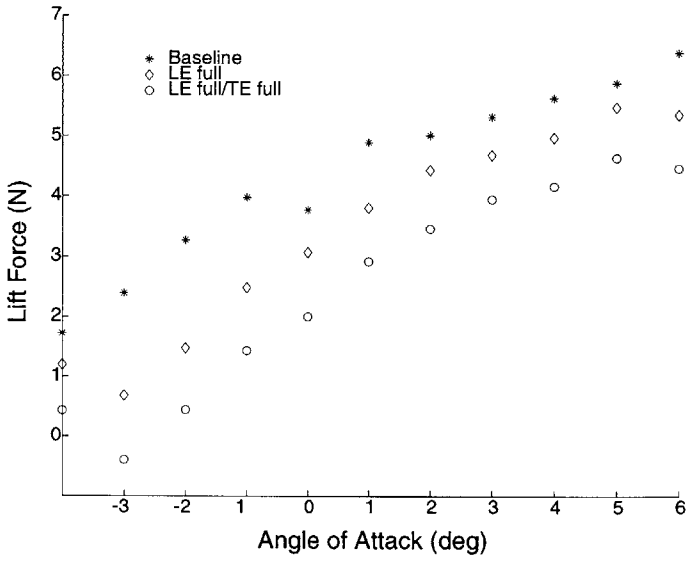


Figure A-5: Lift measurements at 18 m/s

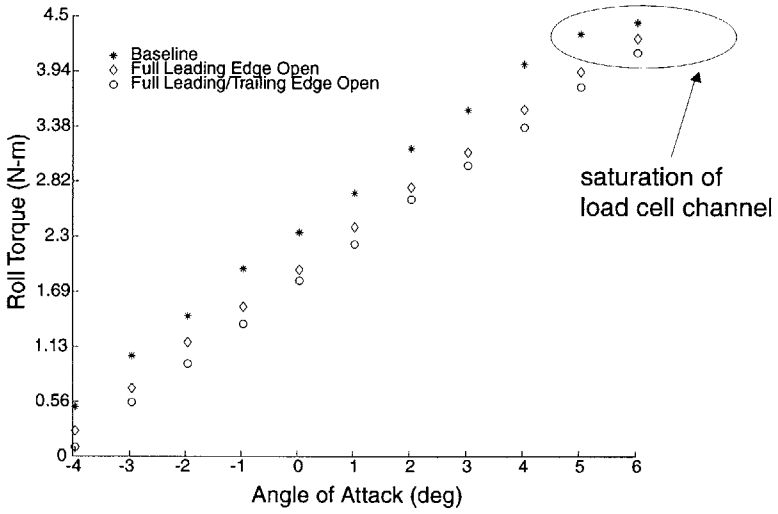


Figure A-6: Torque measurements at 27 m/s

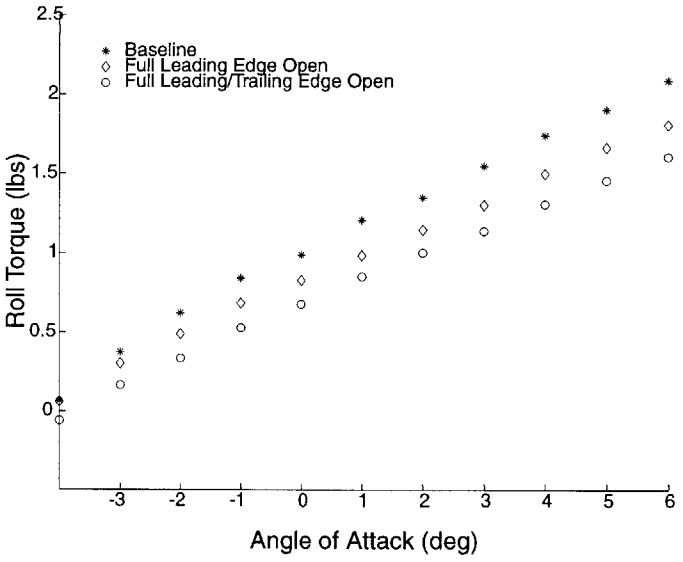


Figure A-7: Torque measurements at 18 m/s

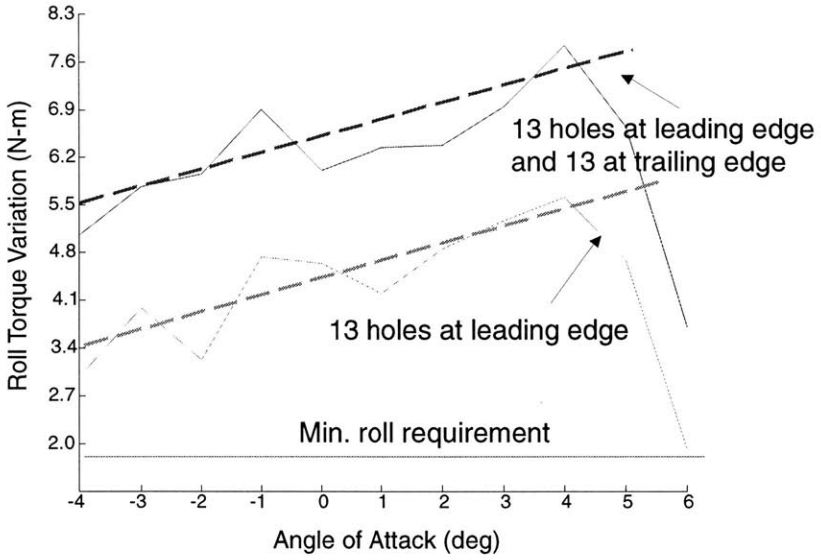


Figure A-8: Net roll measurements at 27 m/s

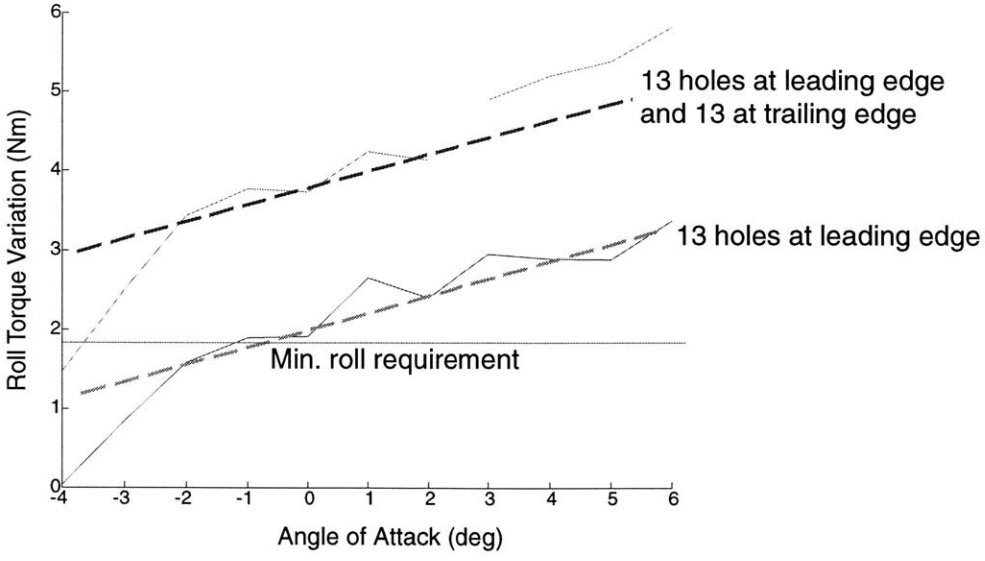


Figure A-9: Net roll measurements at 18 m/s

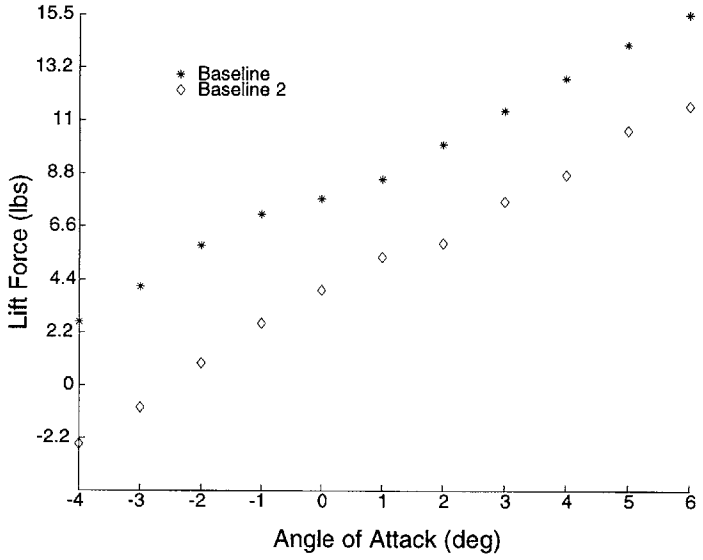


Figure A-10: Baseline lift measurements at 27 m/s

Appendix B

MATLAB Script

The following MATLAB script was used for computing the necessary length of carbon fiber required for the wing fabrication. This script was also used for calculating the mass per unit length of span for a variety of Rohacell cores.

```
clear all

%Input order of polynomial fit
V=input('Order:   ');
%Input Rohacell grade
rohacell=input('Rohacell:   ');
%input layup
plies_upper=input('# of plies upper    ');
plies_lower=input('# of plies lower    ');
%coordinate points of section
A=[0           0
    0.0000    0.0424
         0    0.0447
    0.0001    0.0470
    0.0007    0.0513
    0.0021    0.0566
    0.0038    0.0610
    0.0061    0.0659
    0.0091    0.0713
    0.0131    0.0773
    0.0198    0.0861
    0.0277    0.0951
    0.0381    0.1054
    0.0474    0.1137
    0.0640    0.1270
    0.0799    0.1384
    0.1084    0.1563
    0.1469    0.1771
    0.1937    0.1987
    0.2399    0.2170
    0.2981    0.2367
    0.4028    0.2652
    0.4981    0.2850
    0.5967    0.3007
    0.7087    0.3136
    0.7997    0.3207
    0.9124    0.3258
    1.0115    0.3273
    1.1453    0.3252
    1.2621    0.3200
    1.3681    0.3127
    1.4660    0.3039
    1.5608    0.2938
    1.6495    0.2828
    1.7519    0.2686
    1.8526    0.2530
    1.9243    0.2409
    2.0351    0.2209
    2.1184    0.2049
    2.2150    0.1851
    2.3082    0.1650
    2.4126    0.1414
    2.4837    0.1248
    2.5369    0.1122
    2.5712    0.1040
    2.6008    0.0969
    2.6350    0.0886
    2.6630    0.0818
    2.6967    0.0735
    2.7262    0.0663
    2.7555    0.0590
    2.7845    0.0519
    2.8135    0.0450
    2.8496    0
];
x=A(:,1);
y=A(:,2);
clf
```

```
plot(x,y,'r');
%curve fit to aerodynamic shape
R=polyfit(x,y,V);
hold
f=0;
t=sym('t');
for i=1:V
   f=f+R(i)*t^(V-(i-1));
end
ezplot(f+.04,[0,2.8496])
axis equal
%area under foil
value=int(f+.05,t,0,2.8496);
xsec=eval(value)
arc=0;

B=[2.8496         0
   2.8175         0
   2.7396         0
   2.5973         0
   2.4608         0
   2.3329         0
   2.0186         0
   1.6562         0
   1.3077         0
   0.9484         0
   0.7411         0
   0.5575         0
   0.3470         0
   0.2524         0
   0.1633         0
   0.1082         0
   0.0870         0
   0.0657         0
   0.0554         0
   0.0484         0
   0.0441         0
   0.0408         0
   0.0378         0
   0.0349         0
   0.0287    0.0004
   0.0238    0.0013
   0.0191    0.0029
   0.0150    0.0051
   0.0112    0.0082
   0.0087    0.0111
   0.0056    0.0161
   0.0040    0.0197
   0.0024    0.0246
   0.0014    0.0289
   0.0008    0.0326
   0.0004    0.0365
   0.0002    0.0399
   0.0000    0.0424
        0    0.0447
   0.0001    0.0470
   0.0007    0.0513
   0.0021    0.0566
   0.0038    0.0610
   0.0061    0.0659
   0.0091    0.0713
   0.0131    0.0773
   0.0198    0.0861
   0.0277    0.0951
   0.0381    0.1054
   0.0474    0.1137
   0.0640    0.1270
   0.0799    0.1384
```

```
    0.1084    0.1563
    0.1469    0.1771
    0.1937    0.1987
    0.2399    0.2170
    0.2981    0.2367
    0.4028    0.2652
    0.4981    0.2850
    0.5967    0.3007
    0.7087    0.3136
    0.7997    0.3207
    0.9124    0.3258
    1.0115    0.3273
    1.1453    0.3252
    1.2621    0.3200
    1.3681    0.3127
    1.4660    0.3039
    1.5608    0.2938
    1.6495    0.2828
    1.7519    0.2686
    1.8526    0.2530
    1.9243    0.2409
    2.0351    0.2209
    2.1184    0.2049
    2.2150    0.1851
    2.3082    0.1650
    2.4126    0.1414
    2.4837    0.1248
    2.5369    0.1122
    2.5712    0.1040
    2.6008    0.0969
    2.6350    0.0886
    2.6630    0.0818
    2.6967    0.0735
    2.7262    0.0663
    2.7555    0.0590
    2.7845    0.0519
    2.8135    0.0450
    2.8496    0
];
x_prime=B(:,1);
y_prime=B(:,2);
%calculation of arc length
for j=1:size(x_prime)-1
   arc=arc+(sqrt((x_prime(j)-x_prime(j+1))^2+(y_prime(j)-y_prime(j+1))^2));
end
arc
%calculation of masses
xsec_mass=rohacell*0.000036*xsec+plies_upper*.005*.001708*32.2*(arc-
2.85)+plies_lower*.005*.001708*32.2*(2.85)
span=12;
foam_mass=rohacell*0.000036*xsec*span*16000*2;
carbon_mass=(plies_upper*.005*.001708*32.2*(arc-
2.85)+plies_lower*.005*.001708*32.2*(2.85))*span*16000*2;
mass=xsec_mass*span*16000;
%calculation of mass distribution
slope=mass/span;
nodes_y=[0 .6 1.2 1.8 2.4 3 3.6 4.2 4.8 5.4 6 6.5625 7.125 7.6875 8.25 8.84 9.43 10.02
10.61 11.2 12];
xsec_nodes=18;
distload_back=slope*nodes_y/xsec_nodes
hingemass=.027*2*16000;
distload_forw=(mass+hingemass+nodes_y*slope)/xsec_nodes
hingemass
foam_mass
carbon_mass
total_mass=hingemass+(foam_mass+carbon_mass)
```